


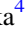






Dissecting the Extended X-Ray Emission in the Merging Pair NGC 6240: Photoionization and Winds

A. Paggi^{1,2,3} , G. Fabbiano⁴ , E. Nardini^{5,6} , M. Karovska⁴ , M. Elvis⁴ , and J. Wang⁷ 
¹ Dipartimento di Fisica, Università degli Studi di Torino, via Pietro Giuria 1, I-10125 Torino, Italy; alessandro.paggi@unito.it
² INAF-Osservatorio Astrofisico di Torino, via Osservatorio 20, I-10025 Pino Torinese, Italy
³ Istituto Nazionale di Fisica Nucleare, Sezione di Torino, via Pietro Giuria 1, I-10125 Torino, Italy
⁴ Center for Astrophysics, Harvard & Smithsonian, 60 Garden St. Cambridge, MA 02138, USA
⁵ Dipartimento di Fisica e Astronomia, Università di Firenze, via G. Sansone 1, I-50019 Sesto Fiorentino, Italy
⁶ INAF-Osservatorio Astrofisico di Arcetri, Largo Enrico Fermi 5, I-50125 Firenze, Italy
⁷ Department of Astronomy, Physics Building, Xiamen University, Xiamen, Fujian, 361005, People's Republic of China
Received 2021 June 23; revised 2022 January 24; accepted 2022 January 28; published 2022 March 14

Abstract

We present a detailed spectral and imaging analysis of the central 15'' radius (~ 7.5 kpc) region of the merger galaxy NGC 6240 that makes use of all the available Chandra-ACIS data (0.3–3 keV effective exposure of ~ 190 ks). This region shows extended X-ray structures with lower-energy counterparts imaged in CO, [O III], and H α line emission. We find both photoionized phases of possible nuclear excitation and thermal shock-excited emission in the different large-scale components: the northwest “loop” detected in H α , the region surrounding the two nuclei, the large outflow region to the northeast detected in [O III], and the southern X-ray extensions. The latter could be the ionization cone of the northern nucleus, with the N counterpart being obscured by the galaxy disk. The radial distribution of the X-ray surface brightness suggests a confined hot interstellar medium at $r < 2.5$ kpc, with a free-flowing wind at larger radii; if the confinement is magnetic, we estimate B -field values of ~ 100 μ G, similar to those measured in the halo of M82. The thermal gas of the extended halo at $kT \sim 1$ keV absorbs soft X-rays from the active galactic nucleus, but not the extreme ultraviolet radiation leading to a rapid increase in $F_{[\text{O III}]}/F_X$ beyond ~ 3 kpc. The α -element to Fe abundance ratios of the thermal components in the different regions of the extended X-ray emission are generally compatible with Type II supernova yields, confirming the importance of active star formation in NGC 6240.

Unified Astronomy Thesaurus concepts: [Active galaxies \(17\)](#); [Interacting galaxies \(802\)](#); [X-ray active galactic nuclei \(2035\)](#)

1. Introduction

NGC 6240 is a highly disturbed merger galaxy at a redshift of 0.0245 ($D = 108$ Mpc, $1'' = 500$ pc; Downes et al. 1993), providing a relatively nearby case study of the complex evolutionary phenomena connected with the merging of galaxies and their nuclear massive black holes. In the optical band, NGC 6240 presents long tidal tails and giant butterfly-shaped H α , and X-ray, emitting loops in the central ~ 15 kpc as well as a disturbed disk crossed by broad dust lanes (Fosbury & Wall 1979; Heckman et al. 1987; Lira et al. 2002; Gerssen et al. 2004). Its strong infrared (IR) emission indicates active merger-induced star formation (Genzel et al. 1998). NGC 6240 contains two well-defined nuclear regions detected at both optical (Fried & Schulz 1983) and IR wavelengths (Scoville et al. 2000). Two highly obscured active galactic nuclei (AGNs) were discovered in this pair of nuclear regions, north (N) and south (S), with Chandra (Komossa et al. 2003) and were subsequently located with high accuracy in radio VLBA images (Gallimore & Beswick 2004). The region near and in between the nuclei is rich in molecular gas (e.g., Tacconi et al. 1999; Treister et al. 2020). Complex kinematics have been reported in both CO and [O III] line emission, suggesting both

nuclear outflows and starburst-induced winds (Feruglio et al. 2013a, 2013b; Müller-Sánchez et al. 2018).

Deep Chandra observations have revealed a rich and complex X-ray morphology, both in the nuclear regions and at larger radii, which we summarize below.

The larger-scale X-ray properties of the merger NGC 6240 are discussed in Nardini et al. (2013). These authors find that the merger resides within a luminous soft X-ray halo (0.4–2.5 keV luminosity of 4×10^{41} erg s $^{-1}$), extending outwards from ~ 7.5 kpc to a projected physical size of $\sim 110 \times 80$ kpc. The halo has a fairly flat radial surface brightness distribution, a radially uniform hot gas temperature of ~ 7.5 million K (0.65 keV), and a total mass of $\sim 10^{10} M_{\odot}$. Because most of the detected photons have energies < 2.5 keV, Nardini et al. (2013) restricted their spectral analysis to this energy range. Modeling the spectral emission of the soft halo with thermal optically thin models, they found that the relative abundances of the main α elements (O, Ne, Mg, Si) with respect to iron are several times the solar value, with no significant radial variations. Nardini et al. (2013) note that the lack of strong radial abundance gradients implies a uniform enrichment by Type II supernovae (SNe II) out to the largest scales. Moreover, the temperature of the halo is significantly higher than expected from a gaseous halo thermalized in the gravitational potential of the system. It is also higher than suggested by merger simulations (expected $kT \sim 0.25$ keV). These results led Nardini et al. (2013) to suggest that a widespread, enhanced star formation, proceeding at a steady



Original content from this work may be used under the terms of the [Creative Commons Attribution 4.0 licence](#). Any further distribution of this work must maintain attribution to the author(s) and the title of the work, journal citation and DOI.

rate over the entire dynamical timescale (~ 200 Myr), contributes to both the energy and metal enrichment of the halo.

Within the inner ~ 7.5 kpc of NGC 6240, Nardini et al. (2013) observe instead a significantly greater surface brightness and higher temperatures (rising to ~ 1.2 keV at ~ 2 kpc), both with steep radial profiles consistent with an expanding adiabatic wind. This is the region with the most disturbed morphology, where tidal effects, the starburst, and the AGN emission are the strongest. Using the full spectral range of Chandra (up to ~ 7 keV), Feruglio et al. (2013b) reported the detection of a hard X-ray emission component in the spectrum from this region. This emission would be consistent with the shock-ionized gas from a nuclear AGN wind matching the terminal velocities of ~ 400 km s $^{-1}$ that they infer from the CO(1–0) line, which they ascribe to nuclear winds from the dual AGN. Wang et al. (2014) also reported extended hard X-ray emission from a $kT \sim 6$ keV (~ 70 MK) hot gas over a spatial scale of 5 kpc, indicating the presence of fast shocks with a velocity of ~ 2200 km s $^{-1}$. Moreover, they mapped the spatial distribution of this highly ionized gas using the 6.7 keV Fe XXV line, which shows a remarkable correspondence with the large-scale morphology of the H2(1–0) S(1) line emission and H α filaments. While not excluding nuclear winds, they note that the propagation of fast shocks originating in the starburst-driven wind into the ambient dense gas can account for this morphological correspondence.

A reanalysis of the innermost $\sim 2''$ (~ 2 kpc) radius region in the hard X-ray, at the highest resolution allowed by the Chandra point response function, was recently reported by Fabbiano et al. (2020). Focusing on the hard-energy bands containing the hard spectral continuum (5.5–5.9 keV), the redshifted neutral Fe K α line (6.0–6.4 keV), and the redshifted thermal Fe XXV line (6.4–6.7 keV), these authors were able to resolve structures with sizes from ~ 1 kpc to < 200 pc. They found significant extended emission in both continuum and Fe lines in the $\sim 2''$ (~ 1 kpc) region surrounding the nuclei, in the region between the N and S AGN, and in a sector of position angle 120° – 210° extending to the SE from the centroid of the S AGN surface brightness. The extended neutral Fe K α emission is likely to originate from the fluorescence of X-ray photons interacting with dense molecular clouds, providing a complementary view to recent high-resolution Atacama Large Millimeter/submillimeter Array (ALMA) studies. The non-thermal emission (i.e., neutral Fe K α) is more prevalent in the region in between the two active X-ray nuclei and in the N AGN.

In this paper, we use the deep (~ 300 ks) coadded Chandra-ACIS data set on NGC 6240 to probe in detail the spatial and spectral properties of the inner ~ 7.5 kpc region. This study is complementary to the work of Nardini et al. (2013), in that it explores this region with the ultimate Chandra spatial resolution. It is also complementary to the work by Wang et al. (2014) and Fabbiano et al. (2020), in that the spectral analysis concentrates on the energy range < 3 keV, where the emission from the extended loops and filaments is particularly strong. This spectral range is sensitive to both thermal emission from the interstellar medium (ISM) (with the exclusion of the strong shocks explored by Feruglio et al. 2013b, Wang et al. 2014, and Fabbiano et al. 2020) and to the nonthermal photoionization emission from the dual AGN (see, e.g., Fabbiano et al. 2018 in the case of ESO 428-G014). After

producing the merged data cube (Section 2), we use subpixel imaging, image enhancement, and reconstruction techniques to provide the most detailed spatially resolved X-ray images of NGC 6240 (Section 3). Based on this image, we perform spectral analysis from selected regions to constrain the emission parameters (Section 4). We discuss the implications of our results in Section 5 and summarize our findings in Section 6.

In this paper, we assume a flat Λ CDM cosmology with $H_0 = 69.6$ km s $^{-1}$ Mpc $^{-1}$, $\Omega_M = 0.286$, and $\Omega_\Lambda = 0.714$ (Bennett et al. 2014).⁸

2. Data Preparation and Analysis Methods

We have used the same data set as in Nardini et al. (2013), Wang et al. (2014), and Fabbiano et al. (2020), which includes all of the available ACIS-S observations with NGC 6240 at the aimpoint. It consists of two imaging ACIS-S observations (ObsID 1590 and 12713) with a total exposure time of 183 ks and of two ACIS-S HETG grating observations (ObsID 6908, 6909) with a total exposure time of 302 ks. The observations were retrieved from Chandra Data Archive through the ChaSeR service.⁹ We use the zeroth-order images of the grating observations. Given the response of the gratings, the combined effective ACIS-S imaging exposure times are ~ 190 ks (0.3–3 keV), ~ 210 ks (3–6 keV), and ~ 360 ks at higher energies.

As in Fabbiano et al. (2020), data have been analyzed with CIAO (Fruscione et al. 2006) data analysis system version 4.12 and the Chandra calibration database, CALDB version 4.9.1, adopting standard procedures.

To optimize the spatial resolution of the data, we use the same merged data set and merged point-spread function (PSF) as in Fabbiano et al. (2020). The data were merged using the peak emission of the strong hard-band dual AGN sources (see Fabbiano et al. 2020 for details on the merging procedure). We used a subpixel binning of $1/16$ of the $0''.492$ ACIS instrumental pixel.¹⁰ This method has been validated by several works, including our own (see, e.g., Harris et al. 2004; Siemiginowska et al. 2007; Karovska et al. 2010; Wang et al. 2011a, 2011b, 2011c; Paggi et al. 2012; Fabbiano et al. 2018). It is conceptually comparable to the Hubble Space Telescope (HST) drizzle imaging (Fruchter & Hook 2002) and exploits the sharp central peak of the Chandra PSF and the well-characterized Chandra dither motion¹¹ to retrieve the full Chandra mirror resolution. Figure 1 compares the $1/16$ pixel full-band (0.3–8 keV) ACIS merged image (left panel) with the 10 ks HRC image (ObsID 438, PI Murray; Lira et al. 2002). The HRC instrumental readout pixel is $0''.1318$, so that the full resolution of the PSF (FWHM $\sim 0''.2$) is exploited.¹² Although the signal to noise of the HRC image is much inferior to that of the long ACIS exposure, the good agreement between the main features of the extended emission demonstrates the validity and power of the $1/16$ pixel imaging. Note that given the softer energy response of the HRC, the two nuclear sources are less prominent than in the ACIS image. These nuclei have large intrinsic absorbing columns (Komossa et al. 2003; Nardini 2017).

⁸ With this cosmology, the redshift of 0.0245 of NGC 6240 corresponds to a luminosity distance of 107.5 Mpc and an angular scale of 496 pc arcsec $^{-1}$.

⁹ <http://cda.harvard.edu/chaser>

¹⁰ https://cxc.harvard.edu/proposer/POG/html/chap6.html#tab:acis_char

¹¹ https://cxc.harvard.edu/proposer/POG/html/chap5.html#th_sEc5.3

¹² https://cxc.harvard.edu/proposer/POG/html/chap4.html#th_sEc4.2.3

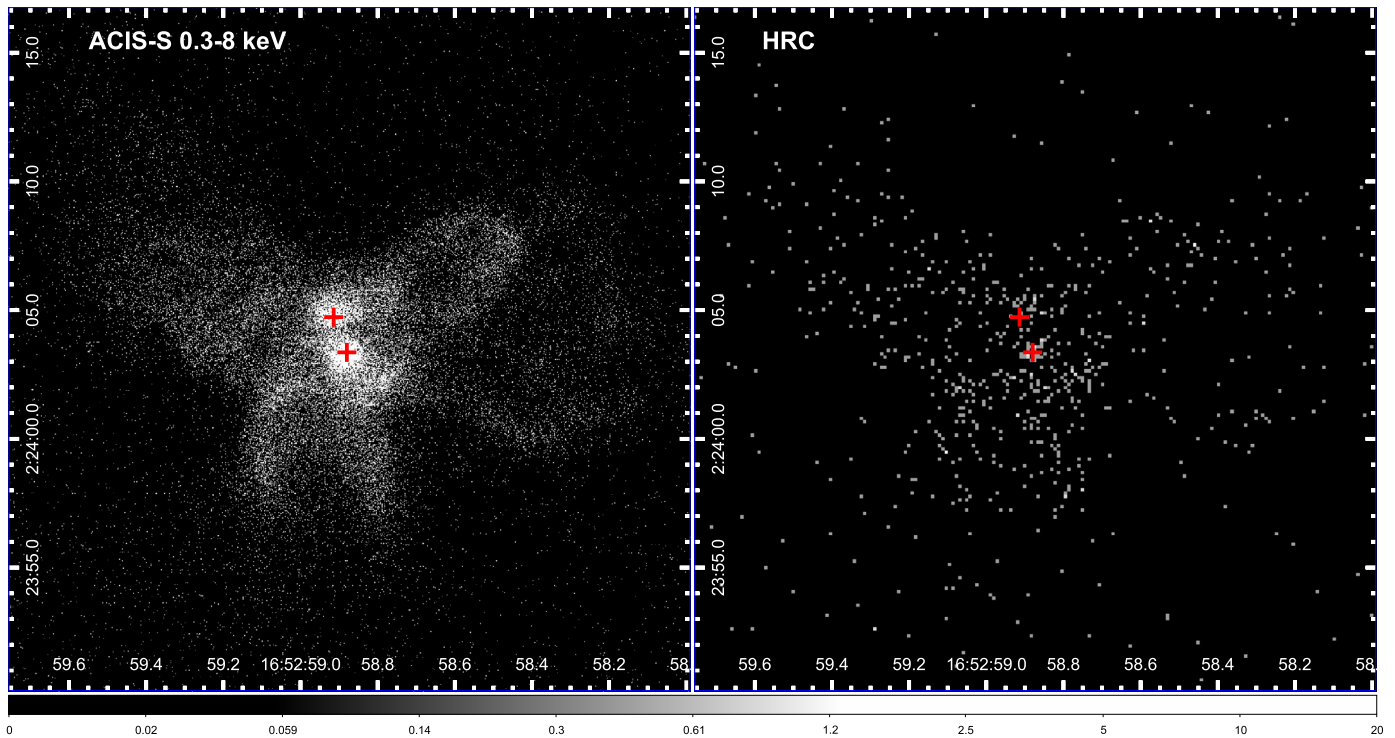


Figure 1. Left: ACIS merged image (0.3–8 keV), with a pixel size of 1/16 ACIS instrument pixel and no image processing. Right: HRC image (ObsID 438). The gray scale gives the logarithmic intensity scale in counts per image pixel. The positions of the nuclear centroids in both images are marked by red crosses.

3. Broadband Imaging

We produced images using two different methods: (1) adaptive smoothing, with the CIAO tool DMIMGADAPT, which uses a range of Gaussian kernels to smooth the data; and (2) image reconstruction, with the image restoration algorithm Expectation through Markov Chain Monte Carlo (EMC2; Esch et al. 2004; Karovska et al. 2005, 2007, 2010; Wang et al. 2014), sometimes referred to as PSF deconvolution) with the PSF models derived in Fabbiano et al. (2020) from the nuclear sources.

To better visualize the extended emission, we have produced adaptively smoothed maps with the CIAO tool DMIMGADAPT. For the full-scale image in the 0.3–3 keV energy band, which contains the line-dominated soft emission (see Section 4), we used 1/8 binned data smoothed with Gaussians, with 16 counts under the kernel and sizes ranging from 1/2 to 30 image pixels, in 30 logarithmic steps, and we also further smoothed the resulting image with a 2 pixel Gaussian. For the 4–7 keV band, where the extended emission has a lower count rate, we followed the same procedure but used 10 counts under the kernel and a 1/16 pixel to better isolate the bright nuclear sources (see Fabbiano et al. 2020).

The left panel of Figure 2 shows the adaptively smoothed image in the 0.3–3 keV band, where the emission spectrum displays clear emission-line features (Section 4). The 0.3–3 keV image reconstructed with the EMC2 algorithm (1/8 pixel, 100 iterations) is shown in the right panel of Figure 2. It shows more vividly all the features suggested by the adaptively smoothed image.

Figure 3 shows the adaptively smoothed image in the 4–7 keV band, where the emission is dominated by a featureless spectral continuum and the 6.4 keV (neutral Fe $K\alpha$) and 6.7 keV (Fe XXV) emission lines (Wang et al. 2014; Fabbiano et al. 2020). These images are displayed in

logarithmic scale to enhance the large-scale, low-surface-brightness emission.

The soft 0.3–3 keV emission is dominated by large-scale extended features. A prominent loop of emission extends to the NW out to ~ 10 kpc from the nuclei, and a long filament is visible to the S of this loop. Two similar-sized prominent protrusions are visible to the S of the nuclei, and a large extended feature with a cross-ridge of enhanced emission is also visible to the NE. These features are highly statistically significant. For example, even the faint “yellow” clumps in the NW quadrant (see Figure 2) contain ~ 100 counts in $\sim 0''.6$ radius circles, compared with the average ~ 50 counts in similar-size regions in the “green” plateau in the same area, resulting in $>4\sigma$ excesses. In the same $0''.6$ radius circle, the “dark blue” regions surrounding the “green” plateau yield ~ 8 counts.

The 4–7 keV image is instead dominated by the two highly absorbed Compton-thick AGNs (CT AGNs) and circumnuclear emission (see Komossa et al. 2003; Wang et al. 2014; Fabbiano et al. 2020). The nuclei are not prominent in the 0.3–3 keV map, where their positions from the 4–7 keV image are shown as crosses. Extended emission is also visible out to ~ 3 kpc radius. This hard emission follows the general footprint of the softer emission (see Figure 2), as has been recently observed in several nearby CT AGNs (e.g., Fabbiano et al. 2017, 2018; Ma et al. 2020; Jones et al. 2021; Travascio et al. 2021).

A zoom-in of the central region is shown in Figure 4, where the data are binned in 1/16 pixel and plotted in a linear scale to better highlight the bright circumnuclear filamentary features, which are especially prominent to the SW of the southern AGN. Again, these features are highly significant, with ~ 400 (the northern filaments) and ~ 1500 (the southern filaments) excess counts over the local intense average extended emission.

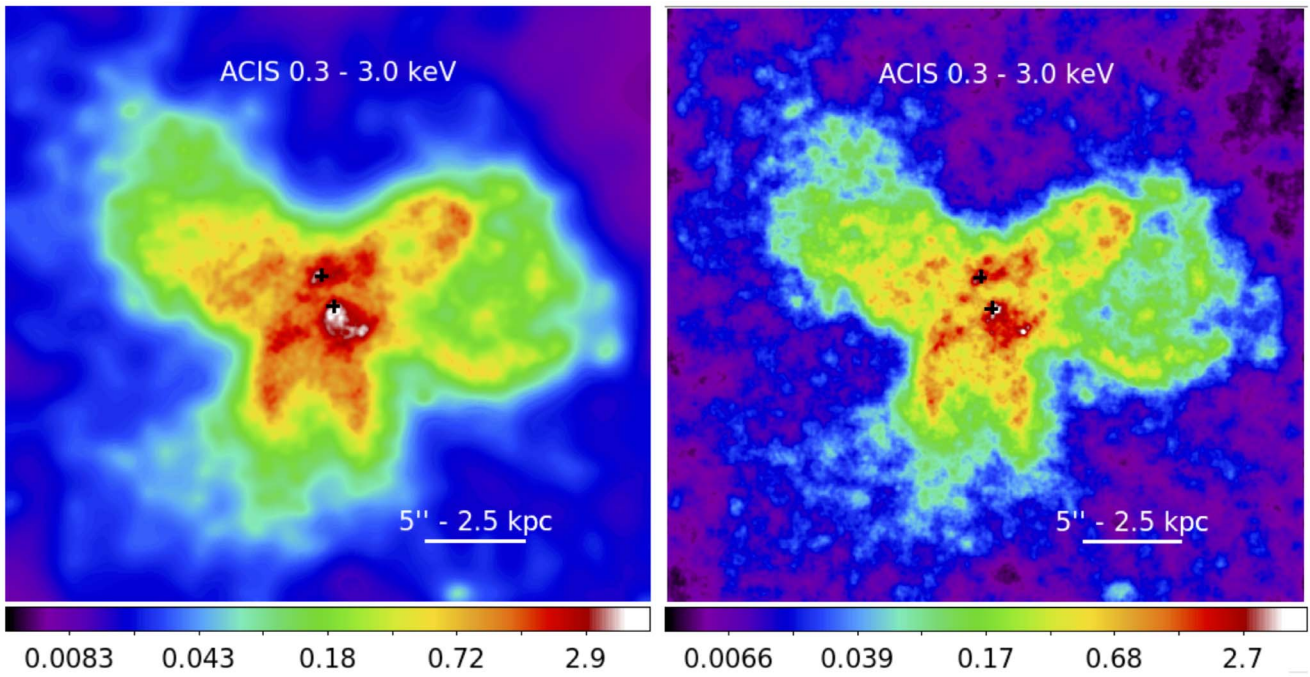


Figure 2. (Left panel) Adaptively smoothed image of the Chandra-ACIS merged data of NGC 6240 in the 0.3–3 keV energy band, with the logarithmic color scale in counts per image pixel (1/8 of the ACIS pixel). (Right panel) EMC2 reconstruction of the same data. N is to the top and E to the left of each image. The crosses are at the peak emission position of the two nuclear sources in the hard-band image (see Figure 3).

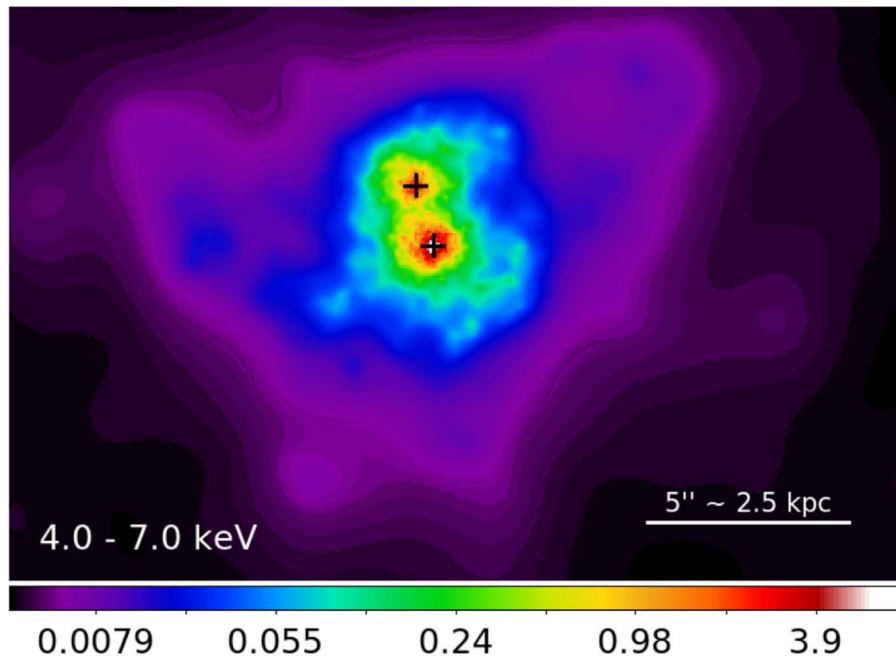


Figure 3. Adaptively smoothed image of the Chandra-ACIS merged data of NGC 6240, in the 4–7 keV energy band. N is to the top and E to the left. The color scale is logarithmic, and the indicated color values at the bottom are in counts per image pixel (1/16 of the ACIS pixel). The crosses are the peak emission position of the two nuclear sources.

4. Spectral Analysis

We performed spectral analysis on several emission regions, using the morphology of the emission as guidance. Given that the morphology of the extended emission is complex (see Figure 2), we do expect that the spectral characteristics may also vary in different regions. We therefore singled out 10 individual regions containing significant morphological features for detailed spectral analysis. These extraction regions all

contain a large number of counts so as to get good spectral constraints. They are shown in Figure 5 and include

1. Two circular regions, which in the hard band are dominated by point-like AGN emission (see Fabbiano et al. 2020; also, Figure 3), denominated as “N nuclear” (2606 net counts in the 0.3–3 keV band) and “S nuclear” (4762 net counts);
2. The surrounding central emission region (nuclear regions excluded, 3924 net counts);

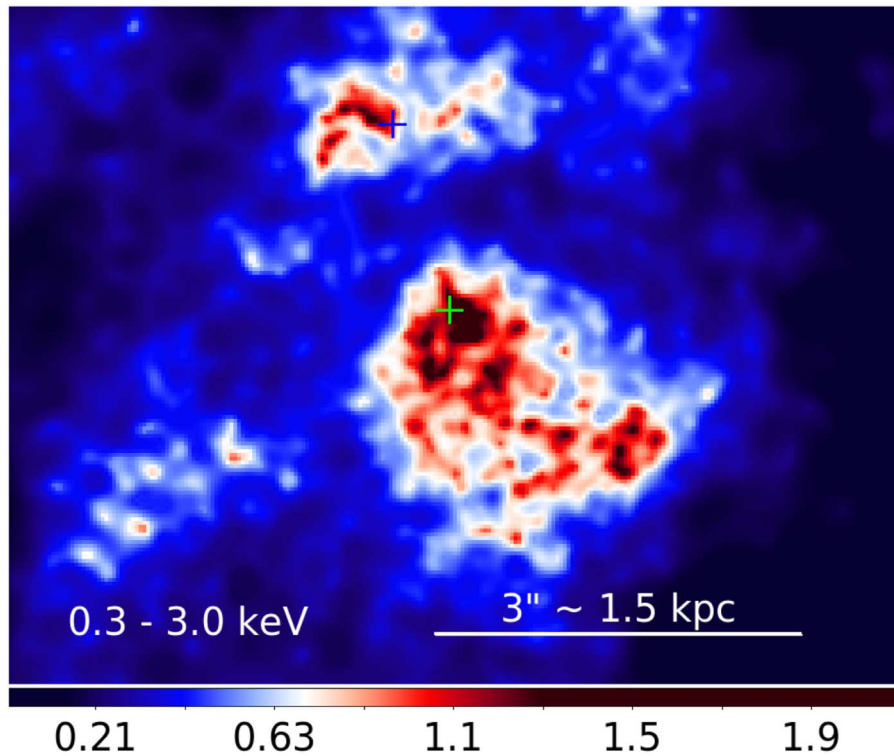


Figure 4. Adaptively smoothed image of the central region of the 0.3–3 keV Chandra-ACIS merged image of NGC 6240 (see the main text). N is to the top and E to the left. The color scale is linear and has been chosen to highlight the filamentary emission. The indicated color values at the bottom of the image are in counts per image pixel (1/16 of the ACIS pixel). The crosses are the peak emission position of the two nuclear sources in the hard-band image (see Figure 3).

3. Two regions in the area where the [O III] emission suggests a nuclear outflow (Müller-Sánchez et al. 2018). These are the “Outer Outflow” region (2844 net counts) and the region at smaller radii where the X-ray image shows a luminous ridge perpendicular to the outflow direction, which could indicate localized shocks (“out-flow ridge,” 2096 net counts).
4. Regions where there are spatially coincident soft X-ray and H α features (see Figure 2; also Lira et al. 2002; Yoshida et al. 2016). These are the two southern extensions, one to the east (“ES extension”—3038 net counts), and the other to the west (“WS extension”—2997 counts); an “NW Loop” (3875 counts); and a “W filament” (1237 counts). We also considered separately the northern continuation of the SW extension, which partially overlaps the central region and presents a strong surface brightness enhancement (“NES extension”—1736 net counts).

We also extracted the spectrum of the entire emission within a circle of radius 15'' (7.5 kpc; encompassing all of the strong extended emission visible in Figure 2), to obtain the overall spectral characterization of the extended emission and in particular to determine the narrowband regions containing the most prominent lines. These lines will then be used for our narrowband mapping of the extended emission (see Section 5.3). This region (named “All”) contains 35,869 net counts in the 0.3–3.0 keV energy band (see below for background subtraction).

For each spectral extraction region, we produced spectral response matrices weighted by the count distribution within the aperture (as appropriate for extended sources). Background spectra were extracted in large ($\sim 80''$), source-free regions in

ACIS-S chip 7, and subtracted from source spectra. We made use of the χ^2 fit statistic, binning the spectra to obtain a minimum of 20 counts per bin. Spectral fitting was performed in the 0.3–3 keV energy range with the SHERPA application (Freeman et al. 2001).

To describe the extracted spectra, we adopted two classes of models.

1. A phenomenological model comprising, in addition to the photoelectric absorption by the Galactic column density along the line of sight $N_{\text{H}} = 5.47 \times 10^{20} \text{ cm}^{-2}$ (HI4PI Collaboration et al. 2016), a power law with photon index fixed to 1.8 and several redshifted Gaussian lines with widths fixed to 10 eV. The 1.8 power law gives a good approximation of the hard AGN emission that may be present in the central regions given to PSF wing spillover (e.g., see Levenson et al. 2006; Fabbiano et al. 2018). The redshift assumed for the emission lines is systemic only (0.0245 for $D = 108$ Mpc). All the lines whose normalization was constrained only with an upper limit were removed from the model. In addition, we included in this model an intrinsic photoelectric absorption at the source redshift.
2. A *physical model* comprising, in addition to the Galactic and intrinsic photoelectric absorptions, up to two thermal plasma components and/or up to two photoionization components. The thermal plasma is represented by a VAPEC¹³ model. In this model, the Fe abundance is left free to vary, while the abundances of the α elements O, Ne, Mg, and Si are linked (but can vary together) during the fit. Because we are interested in the abundance ratio

¹³ <https://heasarc.gsfc.nasa.gov/xanadu/xspec/manual/XSmodelApec.html>

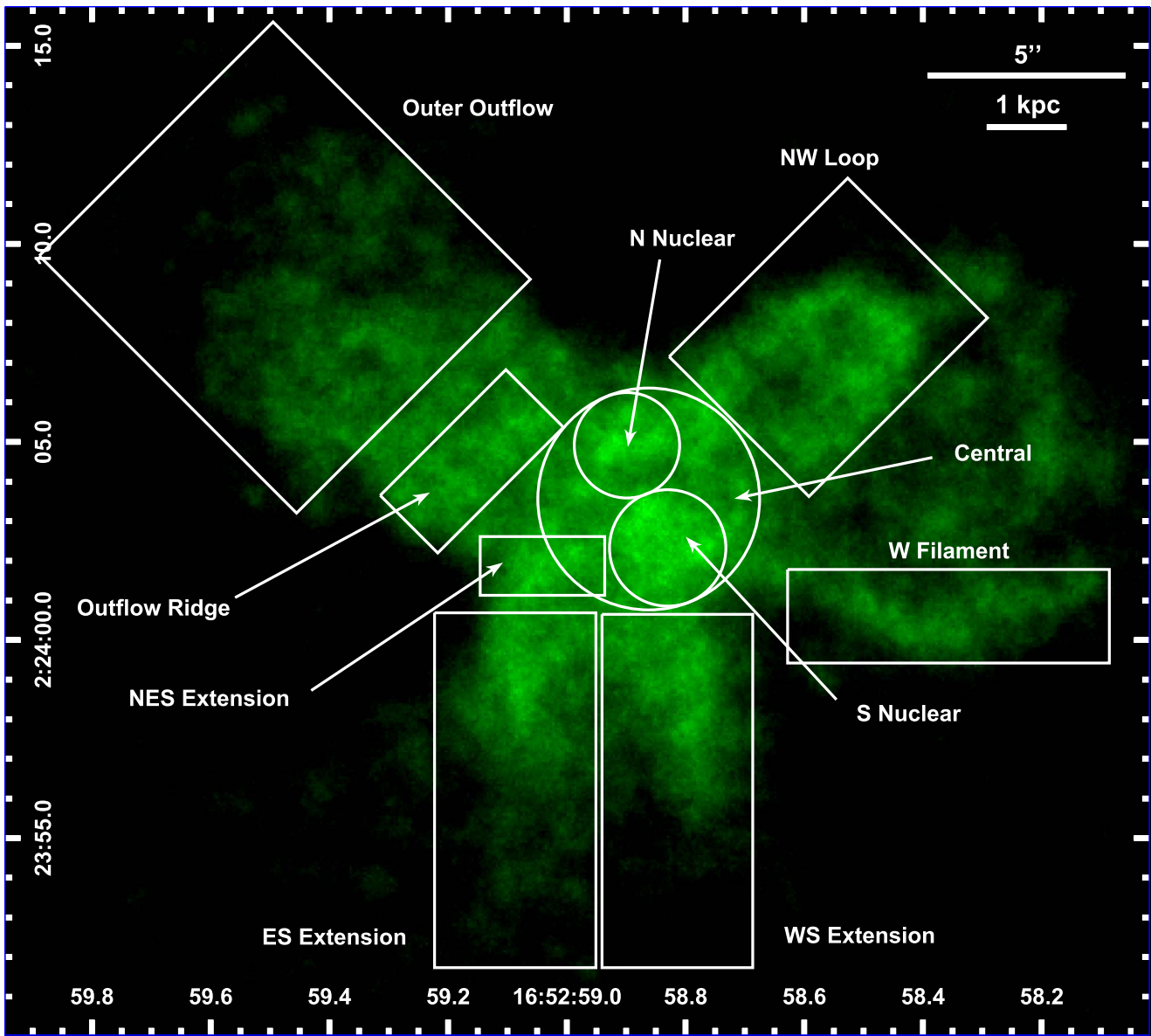


Figure 5. EMC2 reconstructed image of the 1/16 subpixel Chandra-ACIS merged data of NGC 6240 in the 0.3–3 keV energy band, with the spectral extraction regions discussed in Sections 4 and 5.1 overlaid in white. Note that the central region does not include the N nucleus and S nucleus regions.

of the α elements to Fe (which is a diagnostic of the age of the stellar population), we slightly modified the model in order to evaluate this ratio to allow its errors to be directly determined during the fit (Humphrey & Buote 2006). In addition, when two thermal plasma components were included in the model, we linked the Fe abundances and the α /Fe abundance ratios of the two components. For the photoionization components, we produced grid models with the Cloudy¹⁴ c08.01 package (Ferland et al. 1998). We assumed the ionization source to be a typical AGN continuum (with a “big bump” temperature $T = 10^6$ K, an X-ray to UV ratio $\alpha_{ox} = -1.30$, and an X-ray power-law component of spectral energy index $\alpha_x = -0.8$) illuminating a cloud with plane-parallel geometry and constant electron density $n_e = 10^5 \text{ cm}^{-3}$. The grid of models so obtained is parameterized in terms of the ionization parameter U (varying in

the range $\log U = [-3.00: 2.00]$ in steps of 0.25) and the hydrogen column density N_H (expressed in cm^{-2} varying in the range $\log N_H = [19.0: 23.5]$ in steps of 0.1), taking into account only the reflected spectrum from the illuminated face of the cloud (Bianchi et al. 2010; Marinucci et al. 2011).

The results of the spectral fits for the phenomenological model, which includes the best-fit rest-frame energies of the emission lines, are summarized in Table 1. These results are useful for pinpointing the spectral regions of line emission but should not be used to infer “physical” line fluxes, especially in the range < 1.5 keV where several emission lines that cannot be entirely spectrally resolved at the resolution of ACIS (~ 100 eV) could contribute.

Table 2 summarizes the results of the best fits to each single component and the multiple-component physical models for each region and highlights those we suggest as the best fit for each region, as described below. The full set of results for all

¹⁴ <http://www.nublado.org/>

Table 1

Best-fit Results of the Spectra Extracted in the Regions Presented in Figure 5 for the Phenomenological Models Comprising a Power Law with Slope Frozen at 1.8 and Redshifted Gaussian Emission Lines (see Section 4)

Line	Rest-frame Energy (keV)	N Nuclear	S Nuclear	Central	Outflow Ridge	Outer Outflow	NES Extension	ES Extension	WS Extension	W Filament	NW Loop	All
Line Normalization (10^{-5} photons cm^{-2} s^{-1})												
O VII triplet	0.569					0.20 ^{+0.10} _{-0.10}		0.58 ^{+0.58} _{-0.35}				4.47 ^{+3.08} _{-2.52}
Fe XVIII $1s^22s^12p^6 \rightarrow 1s^22s^22p^43p^1$	0.704	23.02 ^{+26.34} _{-14.74}				0.30 ^{+0.06} _{-0.06}		0.33 ^{+0.17} _{-0.12}	0.29 ^{+0.10} _{-0.09}	0.09 ^{+0.04} _{-0.04}		2.47 ^{+0.86} _{-0.77}
Fe XVII $1s^22s^22p^5 \rightarrow 1s^22s^22p^43s^1$	0.771										0.29 ^{+0.12} _{-0.11}	1.72 ^{+0.74} _{-0.71}
Fe XVII $1s^22s^22p^6 \rightarrow 1s^22s^22p^53d^1$	0.826					0.49 ^{+0.05} _{-0.05}		0.34 ^{+0.12} _{-0.10}		0.24 ^{+0.04} _{-0.04}		3.41 ^{+0.84} _{-0.81}
O VIII RRC	0.871	2.55 ^{+2.04} _{-1.38}			0.28 ^{+0.07} _{-0.06}		0.12 ^{+0.13} _{-0.10}	0.39 ^{+0.12} _{-0.10}	0.58 ^{+0.08} _{-0.07}		0.60 ^{+0.10} _{-0.09}	2.05 ^{+0.65} _{-0.64}
Ne IX triplet	0.915					0.43 ^{+0.05} _{-0.05}						4.39 ^{+0.48} _{-0.44}
Fe XX $1s^22s^22p^3 \rightarrow 1s^22s^22p^23d^1$	0.965	1.97 ^{+1.11} _{-0.83}	0.50 ^{+0.21} _{-0.19}		0.16 ^{+0.06} _{-0.06}			0.34 ^{+0.08} _{-0.07}	0.29 ^{+0.07} _{-0.06}	0.15 ^{+0.03} _{-0.03}	0.22 ^{+0.08} _{-0.08}	
Ne X Ly α	1.022	0.63 ^{+0.56} _{-0.43}	0.30 ^{+0.16} _{-0.16}	0.60 ^{+0.11} _{-0.10}	0.17 ^{+0.06} _{-0.06}	0.46 ^{+0.04} _{-0.04}	0.21 ^{+0.08} _{-0.07}	0.34 ^{+0.07} _{-0.06}	0.27 ^{+0.06} _{-0.05}	0.11 ^{+0.03} _{-0.03}	0.60 ^{+0.08} _{-0.08}	4.37 ^{+0.33} _{-0.30}
Fe XVIII $1s^22s^22p^5 \rightarrow 1s^22s^22p^44d^1$	1.095		0.40 ^{+0.11} _{-0.11}		0.12 ^{+0.04} _{-0.04}							0.87 ^{+0.34} _{-0.34}
Fe XXIII $1s^22s^2 \rightarrow 1s^22s^13p^1$	1.129					0.14 ^{+0.02} _{-0.02}			0.25 ^{+0.03} _{-0.03}			0.77 ^{+0.39} _{-0.39}
Fe XIX $1s^22s^22p^4 \rightarrow 1s^22s^22p^34d^1$	1.146			0.14 ^{+0.06} _{-0.06}				0.15 ^{+0.03} _{-0.03}				
Fe XVII $1s^22s^22p^6 \rightarrow 1s^22s^22p^57d^1$	1.180	0.35 ^{+0.20} _{-0.16}	0.10 ^{+0.07} _{-0.07}		0.09 ^{+0.03} _{-0.03}		0.05 ^{+0.03} _{-0.03}			0.05 ^{+0.01} _{-0.01}	0.26 ^{+0.04} _{-0.04}	0.38 ^{+0.23} _{-0.23}
Fe XIX $1s^22s^22p^4 \rightarrow 1s^22s^22p^35d^1$	1.258					0.06 ^{+0.02} _{-0.02}						0.72 ^{+0.12} _{-0.12}
Mg XI triplet	1.352		0.06 ^{+0.05} _{-0.05}	0.13 ^{+0.04} _{-0.04}	0.05 ^{+0.02} _{-0.02}	0.10 ^{+0.02} _{-0.02}		0.08 ^{+0.02} _{-0.02}	0.10 ^{+0.02} _{-0.02}	0.02 ^{+0.01} _{-0.01}	0.21 ^{+0.03} _{-0.03}	0.88 ^{+0.09} _{-0.09}
Fe XXII $1s^22s^22p^1 \rightarrow 1s^22s^12p^14p^1$	1.423						0.05 ^{+0.02} _{-0.02}	0.07 ^{+0.02} _{-0.02}		0.03 ^{+0.01} _{-0.01}		
Mg XII Ly α	1.473		0.13 ^{+0.04} _{-0.04}	0.14 ^{+0.04} _{-0.04}	0.10 ^{+0.02} _{-0.02}	0.06 ^{+0.02} _{-0.02}			0.06 ^{+0.02} _{-0.02}		0.17 ^{+0.03} _{-0.03}	1.00 ^{+0.08} _{-0.08}
Si XIII triplet	1.839	0.14 ^{+0.04} _{-0.04}	0.15 ^{+0.03} _{-0.03}	0.13 ^{+0.03} _{-0.03}	0.08 ^{+0.02} _{-0.02}	0.08 ^{+0.01} _{-0.01}	0.04 ^{+0.02} _{-0.02}	0.07 ^{+0.02} _{-0.02}	0.05 ^{+0.02} _{-0.02}	0.02 ^{+0.01} _{-0.01}	0.16 ^{+0.02} _{-0.02}	1.13 ^{+0.07} _{-0.07}
Mg XII RRC	1.963		0.18 ^{+0.03} _{-0.03}	0.15 ^{+0.03} _{-0.03}	0.05 ^{+0.01} _{-0.01}		0.05 ^{+0.02} _{-0.02}				0.10 ^{+0.02} _{-0.02}	0.64 ^{+0.10} _{-0.10}
Si XIV Ly α	2.006	0.15 ^{+0.03} _{-0.03}										0.23 ^{+0.09} _{-0.09}
S XV Ly α	2.461	0.15 ^{+0.03} _{-0.03}	0.11 ^{+0.03} _{-0.03}	0.11 ^{+0.03} _{-0.03}	0.04 ^{+0.01} _{-0.01}		0.04 ^{+0.02} _{-0.02}	0.02 ^{+0.01} _{-0.01}			0.05 ^{+0.02} _{-0.02}	0.68 ^{+0.06} _{-0.06}
S XIV He β	2.884		0.04 ^{+0.02} _{-0.02}									0.27 ^{+0.05} _{-0.05}
Power-law Norm. (10^{-5} keV $^{-1}$ cm^{-2} s^{-1})		6.27 ^{+0.44} _{-0.42}	6.48 ^{+0.27} _{-0.27}	4.99 ^{+0.21} _{-0.21}	1.24 ^{+0.10} _{-0.10}	0.99 ^{+0.07} _{-0.07}	2.05 ^{+0.14} _{-0.13}	1.53 ^{+0.09} _{-0.09}	1.72 ^{+0.09} _{-0.09}	0.58 ^{+0.05} _{-0.05}	2.48 ^{+0.14} _{-0.14}	27.40 ^{+0.54} _{-0.53}
N_{H} (10^{22} cm^{-2})		1.30 ^{+0.11} _{-0.11}	0.54 ^{+0.03} _{-0.03}	0.49 ^{+0.03} _{-0.02}	0.13 ^{+0.03} _{-0.02}	...	0.36 ^{+0.06} _{-0.05}	0.06 ^{+0.04} _{-0.03}	0.09 ^{+0.02} _{-0.02}	...	0.18 ^{+0.02} _{-0.02}	0.22 ^{+0.02} _{-0.01}
χ^2 (d.o.f.)		0.94(76)	0.84(117)	0.91(108)	1.08(62)	0.94(68)	0.94(54)	0.95(75)	0.98(79)	0.85(41)	0.93(95)	1.07(158)
Net Counts (0.3–3 keV)		2606(51)	4762(69)	3924(63)	2096(46)	2844(53)	1736(42)	3038(55)	2997(55)	1237(35)	3875(62)	35869(189)

Note. For each region, the normalization of each line and of the power-law component, the required intrinsic absorption column density, the reduced χ^2 (with degrees of freedom indicated in parentheses), and the 0.3–3 keV net counts (with the error indicated in parentheses) are presented.

Table 2

Best-fit Results of the Spectra Extracted in the Regions Presented in Figure 5 for the Physical Models Comprising the Thermal and Photoionization Components (see Section 4)

	N Nuclear	S Nuclear	Central	Outflow Ridge	Outer Outflow	NES Extension	ES Extension	WS Extension	W Filament	NW Loop
kT_1 (keV)	$2.32^{+1.41}_{-0.58}$	$1.88^{+1.13}_{-0.21}$	$1.45^{+0.11}_{-0.15}$	$0.88^{+0.12}_{-0.06}$	$0.80^{+0.04}_{-0.04}$	$0.84^{+0.19}_{-0.11}$	$0.84^{+0.07}_{-0.04}$	$1.04^{+0.26}_{-0.06}$	$0.75^{+0.05}_{-0.04}$	$0.82^{+0.11}_{-0.05}$
kT_2 (keV)						$2.15^{+0.58}_{-0.29}$				$1.82^{+0.28}_{-0.28}$
Fe	$1.22^{+4.35}_{-0.75}$	1.0*	$0.22^{+0.11}_{-0.07}$	$0.11^{+0.08}_{-0.05}$	$0.21^{+0.14}_{-0.07}$	$0.33^{+0.28}_{-0.20}$	$0.12^{+0.03}_{-0.03}$	$0.23^{+0.16}_{-0.08}$	$0.10^{+0.04}_{-0.03}$	$0.34^{+0.24}_{-0.13}$
α/Fe	$3.51^{+1.72}_{-1.05}$	$2.57^{+0.60}_{-1.32}$	$5.06^{+1.86}_{-1.29}$	$6.56^{+3.52}_{-2.03}$	$4.02^{+0.83}_{-0.72}$	$2.45^{+3.34}_{-1.19}$	$3.89^{+0.84}_{-0.71}$	$2.89^{+0.80}_{-0.76}$	$4.25^{+1.28}_{-1.03}$	$4.82^{+1.22}_{-0.92}$
$\log(U_1)$	$0.00^{+0.05}_{-0.10}$	$-0.95^{+0.98}_{-0.07}$	$-0.01^{+0.18}_{-0.19}$	$0.08^{+0.33}_{-0.58}$	$-0.50^{+0.78}_{-0.68}$		$-0.50^{+0.28}_{-0.24}$	$0.26^{+0.06}_{-0.16}$		$1.25^{+0.12}_{-0.12}$
$\log(N_{\text{H}1})$	22.4*	$22.10^{+0.86}_{-0.11}$	22.5*	21.7*	22.2*		22.9*	$20.20^{+0.28}_{-0.30}$		22.1*
$\log(U_2)$		$1.43^{+0.12}_{-0.05}$		2.0*	1.9*					
$\log(N_{\text{H}2})$		20.1*		19.0*	19.7*					
N_{H} (10^{22} cm^{-2})	$1.13^{+0.10}_{-0.07}$	$0.69^{+0.16}_{-0.04}$	$0.68^{+0.05}_{-0.04}$	$0.38^{+0.05}_{-0.05}$	$0.09^{+0.03}_{-0.03}$	$0.68^{+0.21}_{-0.18}$	$0.18^{+0.03}_{-0.04}$	$0.40^{+0.05}_{-0.05}$	$0.19^{+0.05}_{-0.04}$	$0.34^{+0.04}_{-0.03}$
χ^2 (d.o.f.)	1.04(79)	0.74(120)	0.70(110)	0.71(66)	0.68(71)	0.72(56)	0.65(81)	0.76(81)	0.73(45)	0.72(98)

Note. Only best-fit models, selected on the basis of fit statistics and residual distribution, are presented here. The full list of models used in this work is presented in the Appendix. For each region, we show the temperature of the first (kT_1) and second (kT_2) thermal components, the iron abundance (Fe), and the abundance ratio of α elements to iron (α/Fe), both linked between the two thermal components, the ionization parameter of the first (U_1) and second (U_2) ionization components, the hydrogen column density of the first ($N_{\text{H}1}$) and second ($N_{\text{H}2}$) ionization components, an additional intrinsic hydrogen column density (N_{H}), and the reduced χ^2 (with degrees of freedom indicated in parentheses). Parameters marked with an asterisk (*) could not be constrained and were frozen to their best-fit values.

the models considered is reported in Table 4. We start with single-component thermal (kT) and photoionization (U) models and then add additional components in each case as required to get an acceptable fit. In some cases, it is not possible to choose a best-fit model based on χ^2 values only. In these cases, we followed an additional criterion (see Fabbiano et al. 2018 for a detailed discussion), which also considers the behavior of the fit residuals in the various spectral subranges. Whenever a given model resulted in a spectral range of correlated residuals, we took this as an indication of the model not dealing adequately with that particular region of the spectrum, and we added spectral components to obtain a more random run of the residuals overall. For the “All” region, we were not able to get acceptable fits to physical models, likely due to the different plasma components that are responsible for the emission in the different regions that end up mixed together in this large extraction region. The elemental abundances derived from the APEC model (see Table 2) are physically motivated within the full set of elements included in the model. The only caution here is that these estimates may underestimate the abundances if large areas of the image including a range of spectral emissions are averaged together. This is because, given the ACIS spectral resolution, a mix of spectra may result in an apparent increase of the continuum emission. This effect was clearly demonstrated in the case of the Antennae galaxy (Baldi et al. 2006a).

Figure 6 shows the spectrum of the “All” region with the best-fit phenomenological model and fit residuals. Based on this figure and on the phenomenological model results (Table 1), we have selected eight narrow spectral bands that we will use for narrowband imaging. These energy bands and the contributing emission lines are listed in Table 3. The spectra, best-fit models, and residuals for the 10 individual regions are shown in Figure 7 (phenomenological model) and Figure 8 (physical models). Figures 7 and 8 clearly show that spectra from different regions may be substantially different. In particular, the N nuclear region has significantly less emission in the softer band (<1.5 keV) than the S nuclear region, suggesting localized higher absorption in this region; the

spectral fits also suggest a larger N_{H} in the N nuclear region (see Tables 1, 2). Note that the AGN emission itself is not contributing directly to the soft band under analysis, given the large intrinsic nuclear absorption columns of these two CT AGNs (Komossa et al. 2003), which instead dominate the emission at energies >3 keV (Figure 3; also Fabbiano et al. 2020). The spectra of the higher-surface-brightness regions (central, NES extension, outflow ridge, NW loop) are relatively harder than those from the regions at larger radii (outflow, ES and WS extensions, W filament).

Below we discuss our results and their implications.

5. Discussion

5.1. Physical Properties of the Hot ISM of NGC 6240

The spectral analysis of the 0.3–3 keV emission shows that the continuum level (represented by the power-law component normalization in the phenomenological model; see Table 1) is comparable in the two nuclear regions. The strongest emission lines in these regions are the Fe XX 3d2p and Ne X Ly α , with the N nucleus showing additional lines at lower energies, in particular strong Fe XVIII and O VIII radiative recombination continuum (RRC) lines. The spectra extracted from the regions closer to the two nuclei—namely the central region and the NES extension—are similar to the nuclear ones, while the spectra from the outermost regions are significantly softer, characterized by lower-energy lines like the O VII triplet, Fe XVIII, and Fe XVII 3d2p. This is consistent with the results from the parameters of the thermal components in the physical model fits (Table 2), which show the presence of a lower-temperature, $kT \sim 1$ keV, gas in the outer regions and a hotter $kT \sim 2$ keV phase closer to the nuclei.

If collisional ionization is the predominant excitation mechanism, these spectral differences suggest stronger shocks in the innermost circumnuclear regions. This would be in agreement with the presence of the previously reported strong Fe XXV line emission in these regions, at 6.7 keV in the rest frame of NGC 6240, which has been connected with strong nuclear winds (velocities of 600 to over 800 km s $^{-1}$; Feruglio et al. 2013a, 2013b)

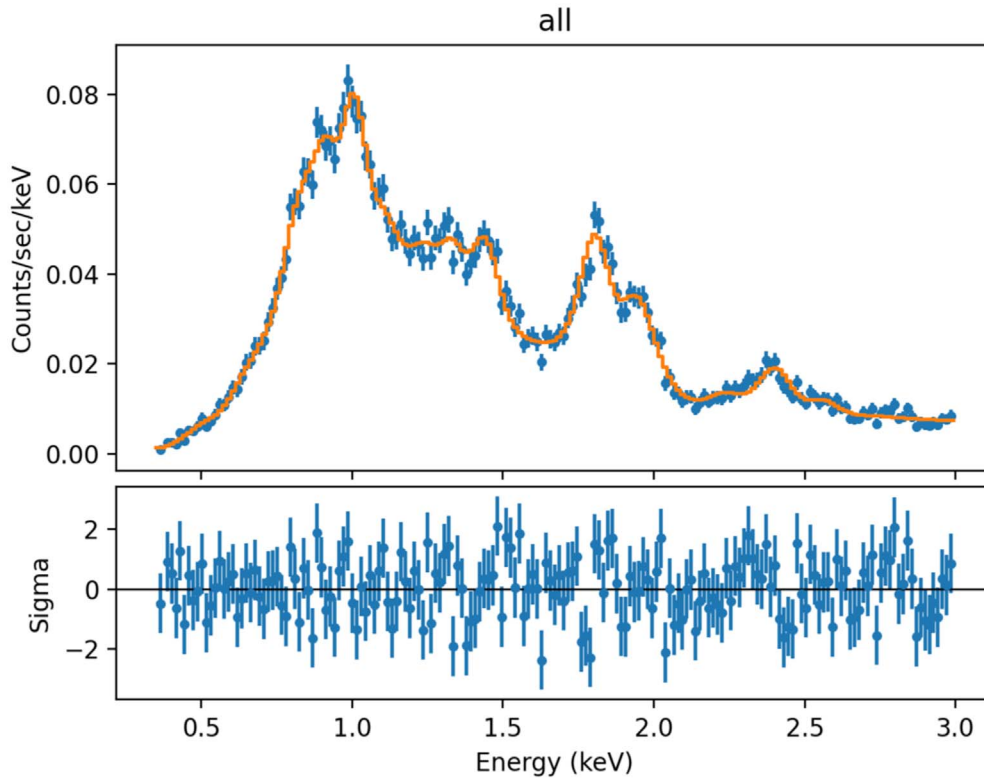


Figure 6. Best-fit phenomenological model (power law plus Gaussian lines) for the spectrum extracted from the central 15'' region (upper panel) and corresponding residuals (lower panel).

Table 3
Lines Contributing to Energy Bands

Energy Band (keV)	Contributing Lines
0.5–0.7	O VII triplet, Fe XVIII
0.7–0.95	Fe XVII, O VIII RRC, Ne IX
0.95–1.15	Fe XX, Ne X, Fe XVIII, Fe XXIII, Fe XIX
1.2–1.4	Fe XI, Mg XI triplet
1.4–1.55	Fe XXII, Mg XII
1.6–1.85	Si XIII triplet
1.9–2.1	Mg XII RRC, Si XIV Ly α
2.2–2.7	Si XV Ly α , Si XIV He β

or also with strong SN shocks in the central active star formation regions of the merger (Wang et al. 2014). The gas masses emitting the X-rays in the major morphological features (e.g., NW loop, outer outflow), estimated from the thermal spectral component emission measure and assuming cylindrical volumes with filling factor 1, are $\sim 1 \times 10^8 M_{\odot}$, with cooling times (30–120) Myr. These are clearly transient events in the lifetime of NGC 6240 as they are comparable to merger timescales (Engel et al. 2010; Treister et al. 2020).

Figure 9 shows the decomposition of the best-fit spectrum extracted in the Central region of NGC 6240 (see Figure 5), with the thermal and photoionization components shown with red and blue lines, respectively. From this figure it appears evident that thermal emission is the dominant process near the double AGN. However, the photoionization component is a nonnegligible contributor to the total emission, accounting for $\sim 20\%$ of the total intrinsic flux.

We have revisited the radial distribution of the X-ray surface brightness using our higher-spatial-resolution images (see the previous work by Nardini et al. 2013 for the full-scale surface brightness profiles at large radii). Figure 10 shows detailed radial profiles of the inner 20'' region of NGC 6240, extracted in the azimuthal bins presented in the upper-left panel. The profiles extracted from the NW cone (containing the H α loop), the NE cone (containing the [O III] outflow), the SE cone (containing the southern X-ray extension), and the SW cone (containing the W filament) are presented in the upper-central, upper-right, lower-left, and lower-central panels, respectively, while the profile extracted from the full 360° sector is presented in the lower-right panel. These profiles all have a broken power-law form, flatter in the interior, and steeper in the outer regions, with the break occurring between $\sim 1''$ and $\sim 5''$. Depending on the azimuthal bins, we find slopes $\sim r^{-\alpha}$ outside 5'' $\alpha_{>5} = 3-4$, while within 5'' we find $\alpha_{<5} = 0.4-0.9$.

Radial dependence of the surface brightness of r^{-3} would result from a radial density dependence of r^{-2} , i.e., freely expanding wind (as discussed, e.g., in the case of M82, Fabbiano 1988; and NGC 6240, Nardini et al. 2013). Possibly steeper slopes, as allowed by the surface-brightness fits for $r > 5''$, may indicate adiabatic cooling of the expanding halo at the larger radii. We note that adiabatic cooling times for the thermal components, despite the large uncertainties, are estimated to be 2–10 Myr, about 5–30 times shorter than the radiative cooling times of 30–120 Myr, estimated from the flux and thermal energy content in the different spectral extractions regions. Therefore, adiabatic cooling is a viable explanation.

The significantly flatter radial dependence of the surface brightness at smaller radii $r < 5''$ shows that the extended X-ray

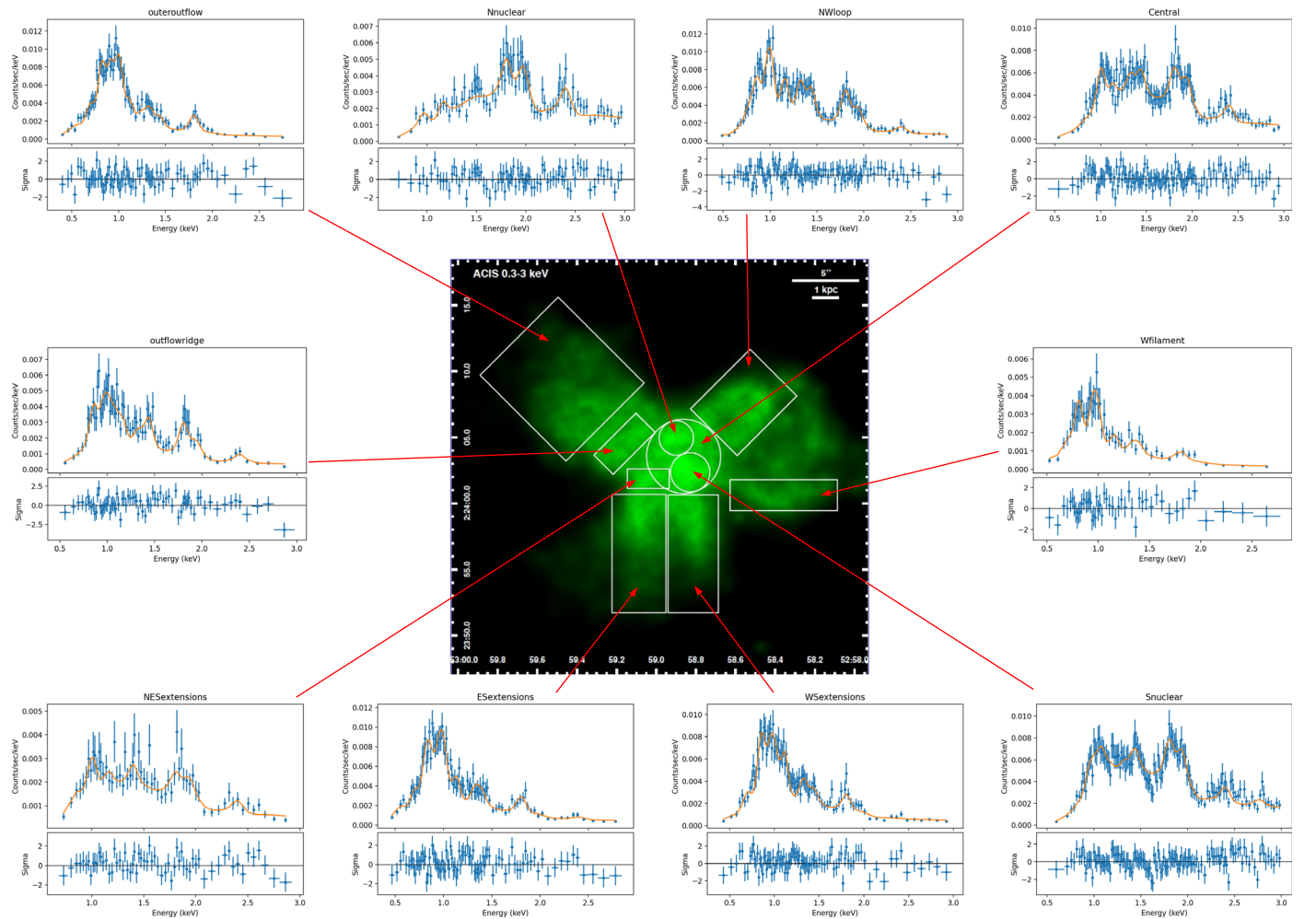


Figure 7. Best-fit spectra for the phenomenological models (power law plus Gaussian lines) for each of the extraction regions presented in Figure 5.

emission in this region is not dominated by a free-flowing wind, suggesting some confinement of the hot plasma in the inner region. By balancing the thermal pressure $P_{\text{th}} = n_{\text{H}} kT / \mu$ (where n_{H} is the thermal gas particle density estimated from the thermal spectral component emission measure, and μ is the mean molecular weight) with the magnetic pressure $P_B = B^2 / 8\pi$ in this inner region, we find that magnetic confinement would require equipartition magnetic fields of the order of $\sim 100 \mu\text{G}$. These fields would be ~ 1 – 2 orders of magnitude larger than magnetic fields measured in the large-scale (~ 100 kpc) X-ray-emitting gas around radio galaxies (e.g., Croston et al. 2005; Simionescu et al. 2008) but lie within the range of the magnetic fields measured in the higher-density \sim kpc scale outflow of the starburst galaxy M82 (a few $100 \mu\text{G}$; Lopez-Rodriguez et al. 2021), a better analogy to the highly disturbed merger NGC 6240.

5.2. Photoionized Emission

We find different ionization parameters in different regions (see Table 2). A mildly photoionized component compatible with $\log(U) \sim 0$ is found both in the N nuclear region and in the ES and WS extension regions (see Section 4 and Figure 5). A more highly ionized component with $\log(U) \sim 1$ is found in the NW loop region, while both photoionization components are found in the S nuclear and in the outer outflow regions. For a similar nuclear photon flux, these differences suggest a range

of cloud densities in the different regions. This may be the case, because the absorbing intrinsic hydrogen column densities estimated with these models are comparable with those estimated from the phenomenological models, being significantly larger in the northern ($1.13^{+0.10}_{-0.07} \times 10^{22} \text{ cm}^{-2}$) and southern ($0.69^{+0.16}_{-0.04} \times 10^{22} \text{ cm}^{-2}$) nuclei with respect to the outer regions, which have $0.39^{+0.13}_{-0.06} \times 10^{22} \text{ cm}^{-2}$ in the outflow ridge. The presence of high-density absorbing clouds in the inner nuclear regions is also demonstrated by the presence of fluorescent neutral iron emission (6.4 keV line) in the high-resolution narrowband Chandra images of the circumnuclear regions and their overall spatial correspondence with molecular line regions imaged with ALMA (Fabbiano et al. 2020).

To shed additional light on the properties of the photoionized medium, we have investigated the properties of the [O III] to soft X-ray (0.5–2 keV) flux ratio, $F_{[\text{O III}]} / F_{0.5-2}$. For a single photoionized medium, this is expected to have an approximately power-law dependence on the radius (assuming constant velocity and mass flux), depending on the radial density profile (Bianchi et al. 2006). In the case of an outflowing nuclear wind, this ratio is expected to be constant (Wang et al. 2011a in NGC 4151).

The upper-left panel of Figure 11 shows the map of $F_{[\text{O III}]} / F_{0.5-2}$. We estimated the [O III] flux from the HST-WFC3 with FQ508N filter image (see Section 5.4) and the 0.5–2 keV flux from the observed Chandra count rates

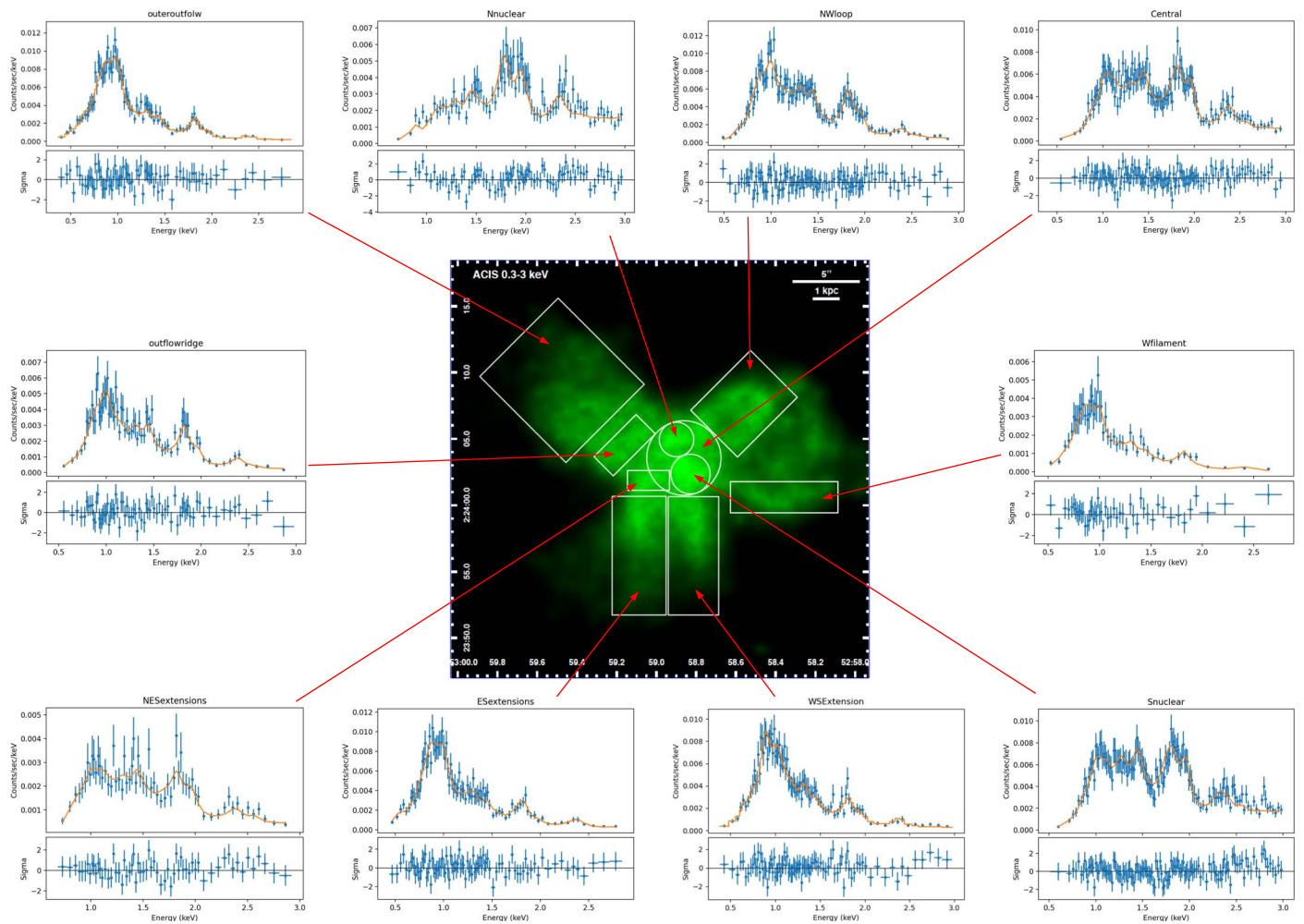


Figure 8. Best-fit spectra for the physical models (thermal gas and photoionization components) for each of the extraction regions presented in Figure 5.

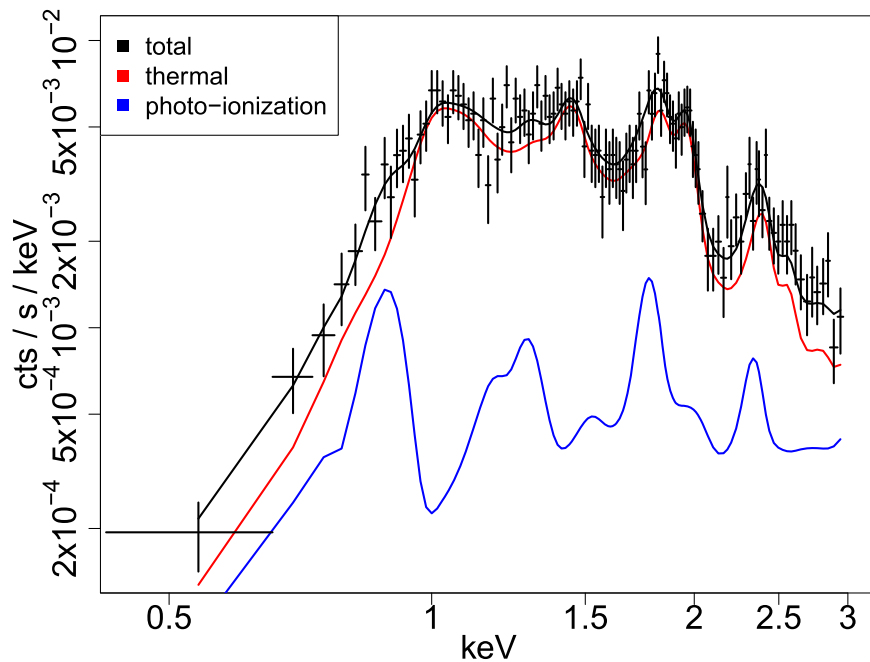


Figure 9. Decomposition of the best-fit spectrum extracted in the central region of NGC 6240 (see Figure 5). The observed spectrum is shown with black crosses, and the best-fit model is presented with a black line. The thermal and photoionization components are shown with red and blue lines, respectively.

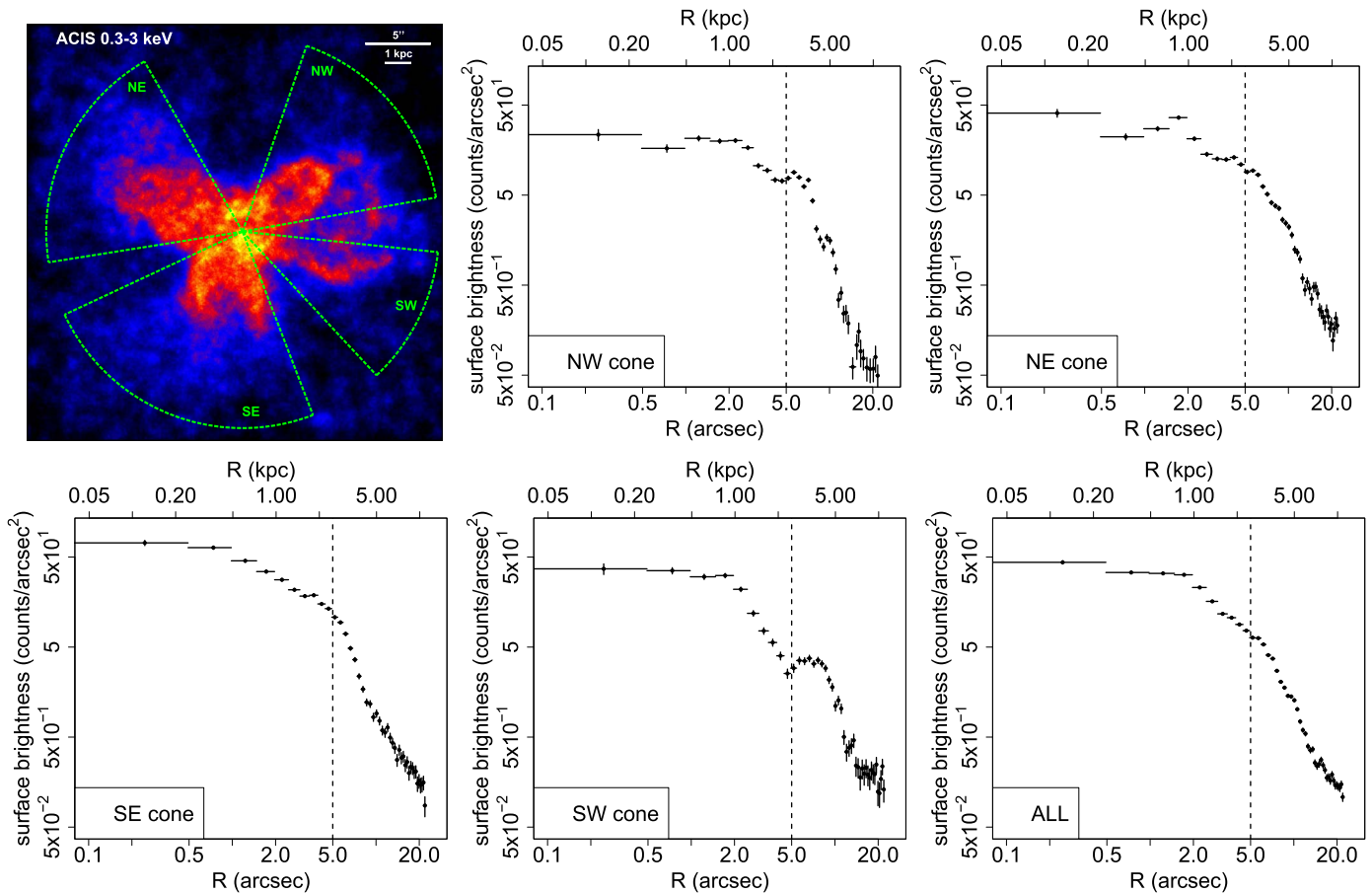


Figure 10. (Upper-left panel) Azimuthal bins used for the surface brightness profile extractions, overlaid on the EMC2 reconstructed image of the 1/16 subpixel Chandra-ACIS merged data of NGC 6240 in the 0.3–3 keV energy band. The surface brightness profiles extracted in the NW cone, NE cone, SE cone, and SW cone are presented in the upper-central, upper-right, lower-left, and lower-central panels, respectively. In the lower-right panel is presented the profile extracted in the full 360° sector. The vertical dashed line marks the $5''$ radius separating the inner and outer profile regions (see main text).

assuming an exposure-weighted average conversion factor of $3.265 \times 10^{-11} \text{ erg cm}^{-2}$ (corrected for Galactic absorption). This map shows that the regions associated with the giant loops and outflow regions have $F_{[\text{O III}]} / F_{0.5-2}$ in the range ~ 15 – 60 (green; see the color scale in Figure 11). These values are comparable to those reported in Seyfert galaxies (Bianchi et al. 2006) and some of the photoionized clouds of NGC 4151 (Wang et al. 2009, 2011a, 2011b). The region within the central $\sim 2.5 \text{ kpc}$ ($r \sim 5''$) shows lower values of the ratio (~ 1 – 8 ; see the blue bins in the figure). These lower values are consistent with those measured in the jet termination regions of NGC 4151, where shock-heated emission is present (Wang et al. 2009, 2011a, 2011b) and would be consistent with the presence of strong thermal emission in these inner regions of NGC 6240 (Section 5.1).

We have superimposed the same azimuthal bins used for the surface brightness profile extraction in Figure 10 on the $F_{[\text{O III}]} / F_{0.5-2}$ map in Figure 11. From these regions we have derived the radial $F_{[\text{O III}]} / F_{0.5-2}$ profiles, also shown in Figure 11. On these profiles, we also plot the values measured at the same physical radii for individual clouds of NGC 4151 by Wang et al. (2011a).

These variations of $F_{[\text{O III}]} / F_{0.5-2}$ within NGC 6240 caution against simple interpretations of the physical state of AGN emitting regions based only on “average” $F_{[\text{O III}]} / F_{0.5-2}$ measurements. In the case of NGC 4151, Wang et al. (2011a) argued that the similarity of the $F_{[\text{O III}]} / F_{0.5-2}$ ratios

measured from individual clouds over a range of radii from $\sim 100 \text{ pc}$ to $\sim 1 \text{ kpc}$ demonstrated the presence of a nuclear wind (excluding the two uncertain measurements and the clouds interacting with the jet, where the $F_{[\text{O III}]} / F_{0.5-2}$ value is lower, because of the additional thermal emission). While we obtain similar values and “flat” $[\text{O III}]/\text{X-ray}$ profiles within $r \sim 5''$ in NGC 6240, both the spectral analysis and the X-ray surface brightness radial profiles in the same regions indicate a prevalent, confined, thermally emitting hot gas (Section 5.1). Moreover, significant structures are evident in the 2D distribution of the $F_{[\text{O III}]} / F_{0.5-2}$ ratio (Figure 11).

At radii $r > 5''$, Figure 11 shows that the $F_{[\text{O III}]} / F_{0.5-2}$ ratio increases almost monotonically as the X-ray flux decreases (Figure 10), reaching a value of ~ 100 at a radius of $\sim 20''$ ($\sim 10 \text{ kpc}$). At these large radii, the X-ray emission is dominated by the thermal emission of an expanding halo (Section 5.1; Nardini et al. 2013).

The observed $F_{[\text{O III}]} / F_{0.5-2}$ ratio should then decrease as $F_{0.5-2}$ is being overestimated, and the photoionized $F_{[\text{O III}]} / F_{0.5-2}$ should be constant (Wang et al. 2009, 2011a), contrary to our results. The observed increase could be due to an intervening warm, partially ionized column of gas that gradually absorbs the AGN photoionizing X-rays while letting through the UV that excites the $[\text{O III}]$ emission (Halpern 1984). Similar ratios were seen in NGC 4151 at the edges of a bicone where additional absorption is plausible (Wang et al. 2009; see the two high-value points in Figure 11). Note that this absorber

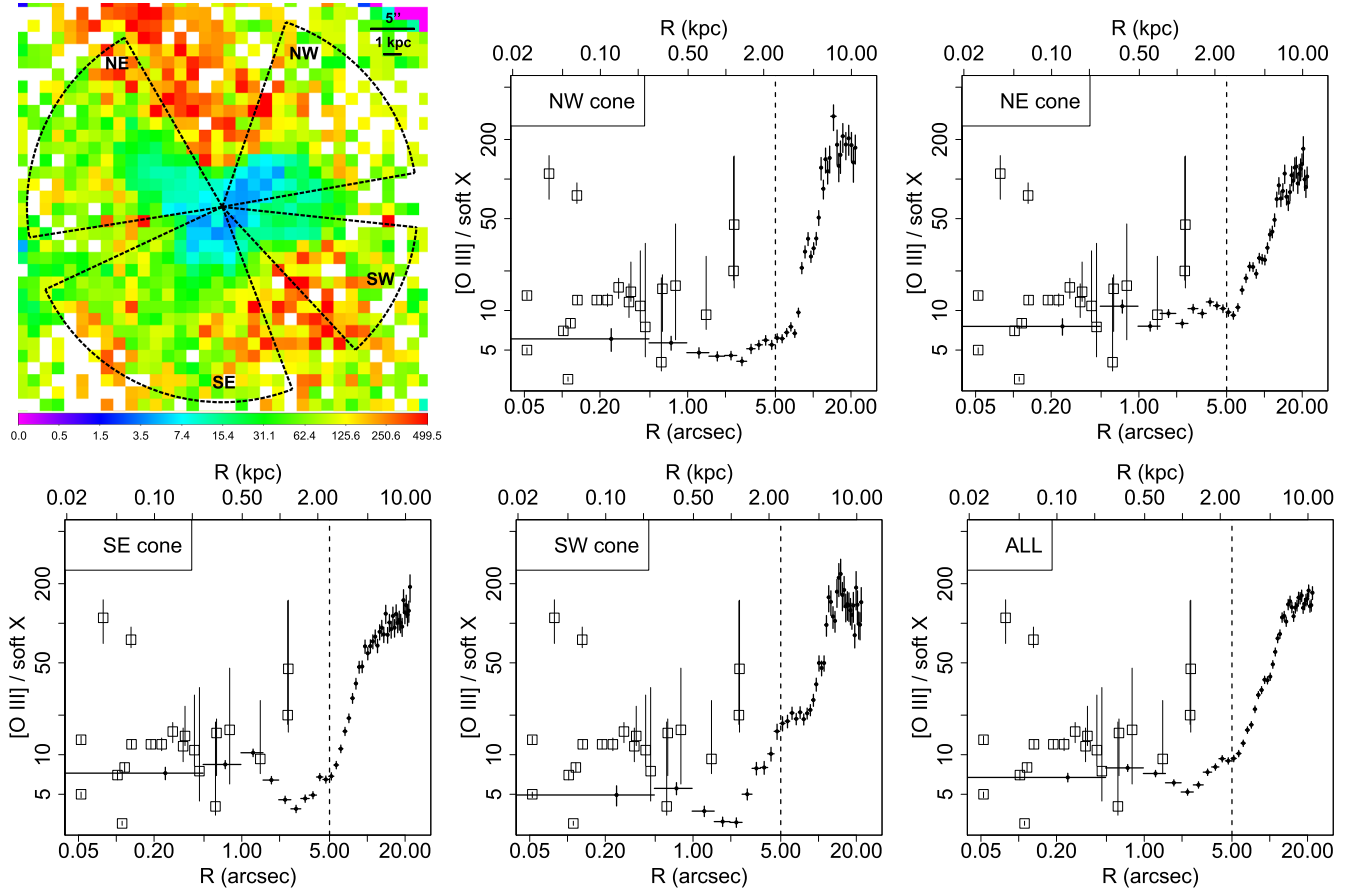


Figure 11. (Upper-left panel) Map of the [O III] to soft X-ray flux ratio, with the same azimuthal bins used for the surface brightness profile extraction superimposed (see Figure 10). The map is binned to a pixel size 20 times that of HST-WFC3 with the FQ508N filter image (see Figure 13). The white pixels represent infinite values of the flux ratio (i.e., zero X-ray flux). The flux ratio profiles extracted in the NW cone, NE cone, SE cone, and SW cone are presented in the upper-central, upper-right, lower-left, and lower-central panels, respectively. In the lower-right panel is presented the profile extracted in the full 360° sector. The vertical dashed line marks the $5''$ radius separating the inner and outer profile regions. The squares represent the ratios measured by Wang et al. (2011a, 2011b) in NGC 4151.

is different from the cold absorber seen in the nuclei. To produce the observed gradual increase in $F_{[\text{O III}]} / F_{0.5-2}$, this absorber must be distributed over the $\sim 5''$ – $20''$ region. Once the thermal emission dominates, however, this explanation is insufficient. A candidate for this putative warm absorbing medium is the thermally emitting hot gas at $kT \sim 1$ keV seen in the region. Its density, evaluated from the emission measure of the spectral thermal components, is in fact $\sim 0.4 \text{ cm}^{-3}$, corresponding to a column density of $\sim 3 \times 10^{21} \text{ cm}^{-2}$ integrated radially along the inner $5''$, which is in the right range to absorb ~ 1 keV X-rays.

5.3. Narrowband Imaging

Our spectral analysis (Section 4) has shown differences in the emission-line properties from different regions of NGC 6240. Using the spectral data as a guide, we have produced images to study the finer-scale morphology of the X-ray line emission using several narrow spectral bands. Given the limited energy resolution of ACIS (~ 100 eV) we cannot image the emission in individual lines, which are often spectrally blended. However, we can use the integrated spectrum of Figure 6 to select different emission features for imaging. The bands chosen for imaging, together with the emission lines that contribute to the emission, are listed in Table 3, while the

resulting narrowband images are presented in the various panels of Figure 12.

Comparison of the images in the different spectral bands shows that:

- The emission features are more prominent at larger radii (outside the central ~ 2 kpc) for the lower energies (< 0.95 keV). This could be due to both the lower AGN excitation of the ISM because of the Compton-thick nuclear obscuration and also an effect of larger line-of-sight N_{H} in the dustier central regions, as suggested by the large $\sim 3 \times 10^{10} M_{\odot}$ molecular mass gas estimated in these regions with ALMA data (Treister et al. 2020).
- The outer outflow [O III] region (Müller-Sánchez et al. 2018) appears to be more smoothly elongated at energies < 0.95 keV, where the O VII, O VIII, and Ne IX lines contribute to the emission, than at higher energies. In particular, the outflow ridge perpendicular to the outflow axis is particularly prominent at ~ 1 keV, and this region is the principal contributor to the emission at higher energies, consistent with the spectral results (Section 4, compare the outer outflow and the outflow ridge spectra). The relatively strong ridge emission in the 0.95–1.15 keV band is interesting because this is the spectral band to which the Ne X line contributes. O VII, O VIII, Ne IX, and Ne X line emission are related to strong shock excitation in nearby

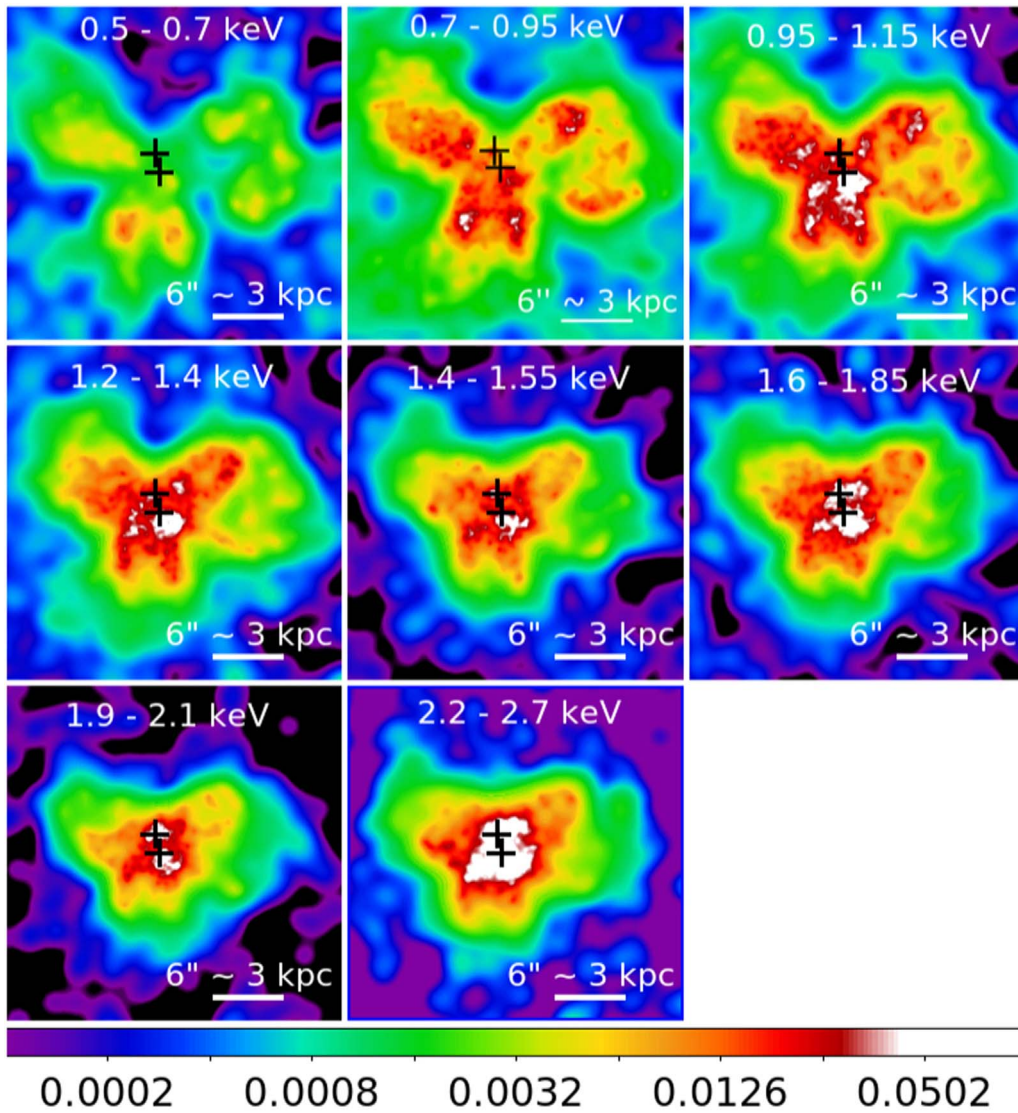


Figure 12. Narrowband images of the 1/16 pixel merged data (see the main text). The energy band is indicated in each panel. The data were adaptively smoothed with 10 counts under the Gaussian kernel; a range of kernels from 1 to 30 image pixels and 30 iterations were used in all cases. The color scale gives the logarithmic intensity scale in counts per image pixel, which was set to be the same for each panel, in order to highlight the larger-scale lower-surface-brightness features. N is to the top and E to the left of each image. The crosses are the peak emission position of the two nuclear sources in the hard-band image (see Figure 3).

Seyfert galaxies (Wang et al. 2010; Paggi et al. 2012; Fabbiano et al. 2019; Maksym et al. 2019) from interaction with radio jets. In the case of NGC 6240 we speculate that this emission may be generated by the interaction of the fast nuclear wind ($\sim 800 \text{ km s}^{-1}$, Feruglio et al. 2013a, 2013b), or star-formation-energized outflow (Wang et al. 2014) with local dense molecular clouds.

- (c) The large NW loop traced by $\text{H}\alpha$ emission (Feruglio et al. 2013a; Müller-Sánchez et al. 2018) has its X-ray emission peaking between 0.7 and 1.15 keV, dominated by O VIII and Ne X emission lines. This structure is also detected at higher energies, with the contribution of Mg XI, Si XIII, and S XV lines, usually associated with starburst activity (Schurch et al. 2002; Persic & Rephaeli 2002). The W filament is mainly detected between 0.7 and 1.15 keV, and it appears dominated by iron lines (Fe XVIII, Fe XVII, and Fe XX).
- (d) The two arms protruding southwards—namely the ES extension and the WS extension—both peak between 0.7

and 1.15 keV, being dominated by O VIII, Fe XX, and Ne X emission. The physical model suggests, for these two regions, the presence of a thermal gas component (with $kT \sim 0.8 \text{ keV}$ and $kT \sim 1 \text{ keV}$ for the ES and WS extension, respectively) with an additional mildly photoionized component in both regions, possibly related to the activity of the northern nucleus (Müller-Sánchez et al. 2018).

The picture that results from these narrowband images is the following:

1. The northern nucleus is characterized by a mildly photoionized component with $\log U \sim 0$, and the same component is found in the ES and WS extension, dominated by O VIII and Ne X lines. These two southern extensions may delineate the edges of the ionization cone originating from the northern nucleus, where the nuclear wind interacts with the local dense ISM. There is no counterpart to this half-bicone to the N, which is unusual in CT AGNs (Fabbiano & Elvis 2019).

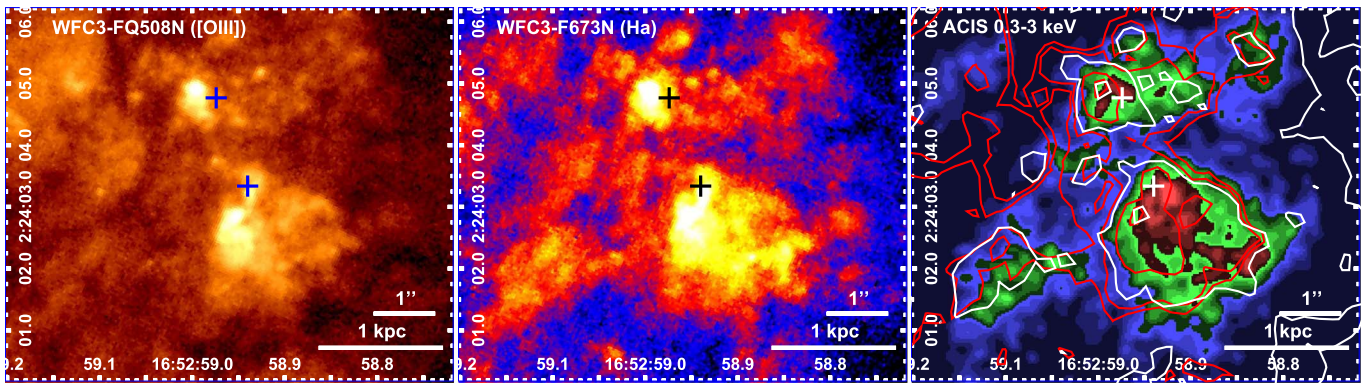


Figure 13. The central region of NGC 6240 (see Figure 2) as imaged by HST-WFC3 with the FQ508N filter (left panel), HST-WFC3 with the F673N filter (center panel), and by Chandra/ACIS-S in the 0.3–3 keV band (right panel). In the right panel, we overlap with the adaptively smoothed Chandra map the contours of the [O III] and H α emissions, represented by red and white lines, respectively. The crosses are the peak emission position of the two nuclear sources in the hard-band image (see Figure 3).

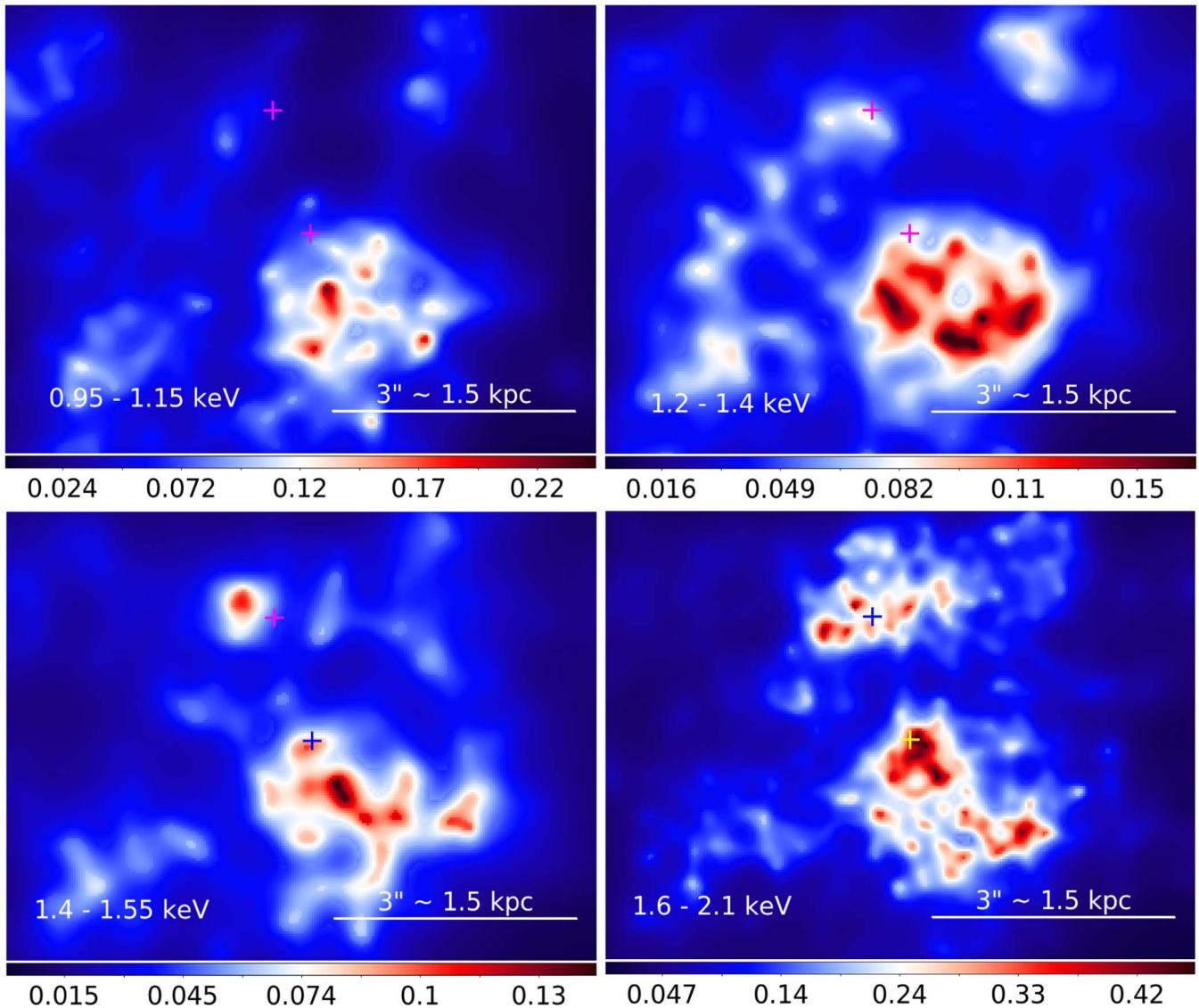


Figure 14. Narrowband images of the inner ~ 2 kpc region (see main text). The energy band is indicated in each panel. From top left, these bands approximately correspond to Ne X, Mg XI, Mg XII, and Si XIII–XIV emission lines. The data were adaptively smoothed with 10 counts under the Gaussian kernel; a range of kernels from 1 to 30 image pixels and 30 iterations were used in all cases. The color scale is linear in all panels, to emphasize the higher-surface-brightness filaments. The intensity scales are in counts per image pixel. N is to the top and E to the left of each image. The crosses are the peak emission position of the two nuclear sources in the hard-band image (see Figure 3).

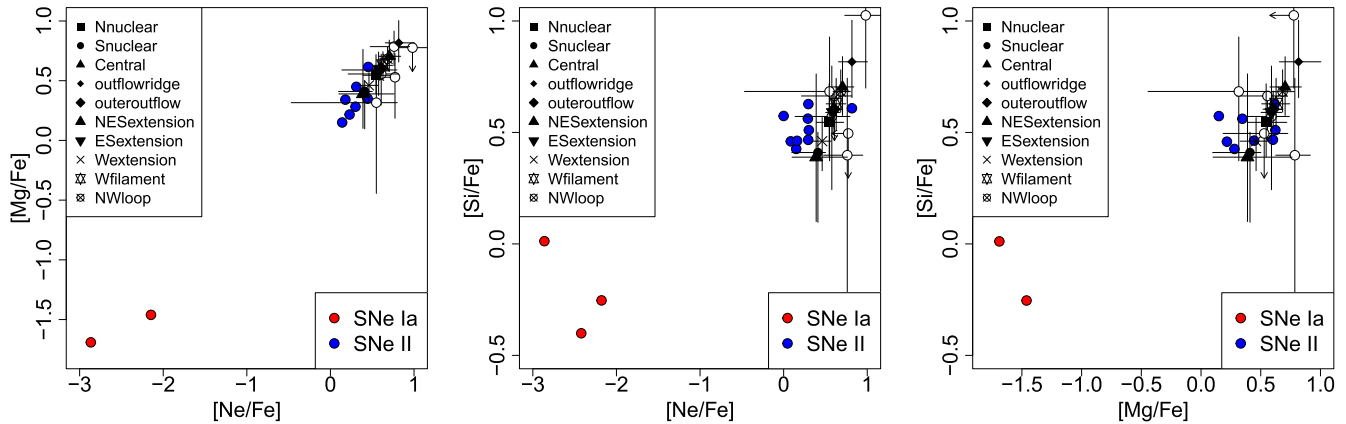


Figure 15. Ratios of the abundances of the α elements to the iron abundance evaluated from the spectral fitting in the extraction regions presented in Figure 5 (black symbols). White circles represent the results from Nardini et al. (2013), with upper limits indicated with arrows. The expected yields from SNe Ia and SNe II are presented with red and blue circles, respectively (Baldi et al. 2006b).

2. The southern nucleus shows an additional photoionization component with $\log(U) \sim 1$ that is also found in the outer outflow region and in the outflow ridge, with these regions being dominated by O VII, O VIII, Ne IX, and Ne X line emission, which are associated with strong shock excitation. This suggests a photoionized outflow from the southern nucleus, where the fast, outflowing nuclear wind (Feruglio et al. 2013a, 2013b; Wang et al. 2014) is pushing out preexisting ISM clouds and giving rise to shock ionization in denser regions. As for the northern nucleus, there is no corresponding W cone.
3. The H α NW loop emission is also modeled with a $\log(U) \sim 1$ photoionization component; however, the strong Mg XI, Si XII, and S XV lines detected here suggest that starburst activity is dominant in this region.

5.4. Inner 2 kpc Emission

Figure 13 shows the ~ 2 kpc central region of NGC 6240 as imaged by HST-WFC3 with the FQ508N filter (left panel), HST-WFC3 with the F673N filter (center panel), and by Chandra/ACIS-S in the 0.3–3 keV band (right panel; see also Figure 4 for a more detailed representation of the 0.3–3 keV ACIS data in the inner region). The regions around the two nuclei show a close resemblance of the morphology of the optical line emission to the overall soft X-ray emission, including the arc to the S and SW of the southern nucleus. While these morphological similarities may suggest a similar emission mechanism, there are subtle differences in both the optical and X-ray emission that support a more complex picture.

Figure 14 shows a different morphology of the X-ray emission as a function of energy. The northern nucleus becomes visible at higher X-ray energies with respect to the southern one (see also Figure 5 in Nardini 2017), consistent with the higher absorbing column estimated for the former (see Section 5.1). Circumnuclear emission for the northern nucleus appears at energies > 1.6 keV, while for the southern nucleus, this is already visible above 0.95 keV. The X-ray and H α region to the SE does not have a comparably strong [O III], suggesting a star formation origin. There is an X-ray arc $\sim 1''$ south of the southern AGN that appears different at different

energies, suggesting either local differences in cloud densities or different local conditions of interstellar shocks. The arc may also result from the counterpart to the outflow in the northeast that, instead of escaping to large radii, interacts with molecular clouds in the region, preventing a large-scale bicone from forming on this side. There is no similar feature corresponding to the counterpart of the northern nucleus outflow that complements the ES+WS outflow to the north. This could be because of obscuration from the galactic disk (see Figure 1 of Müller-Sánchez et al. 2018).

5.5. Metal Enrichment of the Hot ISM

Chandra-ACIS spectra of galaxies have been used to constrain the metal abundances in the hot ISM. In particular, in merging and interacting galaxies, the metal abundance of α elements (O, Ne, Mg, Si) has been found to exceed the solar values, with ratios relative to Fe typical of the yield of SN II (see the Antennae, Baldi et al. 2006a, 2006b; NGC 4490, Richings et al. 2010). These results are consistent with active star formation occurring in these galaxies, leading to the fast evolution of the most massive stars and the consequent SN II explosions. The extended halo of NGC 6240 was found to be enriched in α elements (Nardini et al. 2013), leading to a picture of α -element-enriched winds propagating from the internal active region to the surrounding gaseous halo of this system.

In this paper we studied the region where star formation activity is currently occurring as the result of the merging interaction. Table 2 shows that the iron abundance of the thermal components is found to be about solar in the nuclear regions, while it is lower in the NES extension, WS extension, and NW Loop regions (~ 0.3 solar) and especially so in the outflow ridge, outer outflow, ES extension, and W filament regions (~ 0.1 solar), consistent with the values reported by Nardini et al. (2013). The ratios of the abundance of α elements to iron are found to be $\gtrsim 2$ in all the regions considered in the present analysis. In Figure 15, we plot these ratios and compare them with values obtained by Nardini et al. (2013), which appear to be consistent. We also compare our results with the expected yields by SNe Ia and SNe II (Baldi et al. 2006b and reference therein). This figure shows that the ratios are consistent with SN II—and strongly inconsistent with SN Ia

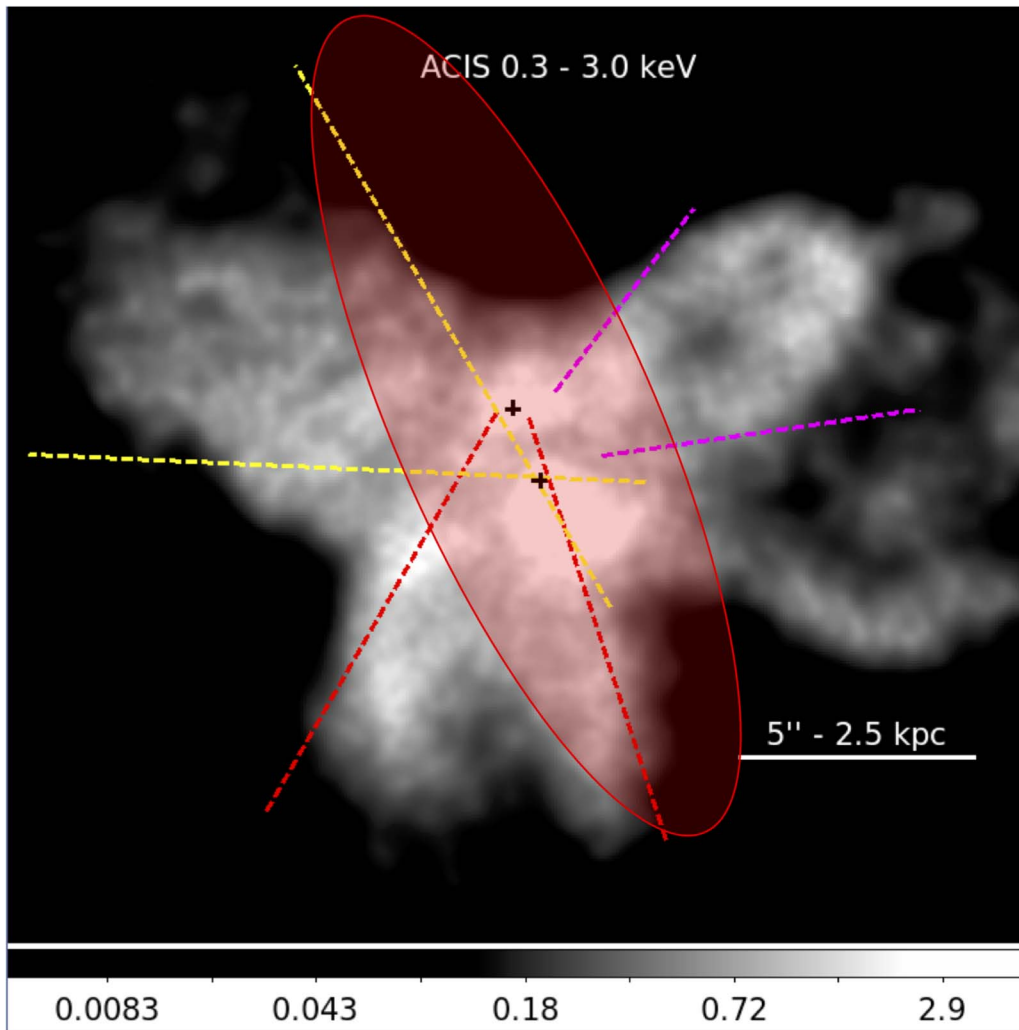


Figure 16. Sketch of the extended X-ray emission observed in NGC 6240. The red dashed lines indicate the edges of the ionization cone connected to the northern nucleus, the yellow dashed lines indicate the edges of the ionization cone linked to the southern nucleus (possibly extending to the west), and the dashed magenta lines indicate the starburst-driven winds yielding the NW $H\alpha$ loop.

—yields for all the regions we have studied spectrally in NGC 6240, in agreement with the results of Nardini et al. (2013) for the outer halo.

6. Summary and Conclusions

We have presented a detailed spectral and imaging analysis of the central $15''$ (~ 7.5 kpc) radius region of the double-AGN merger galaxy NGC 6240 using the complete available Chandra-ACIS data set. This consists of two imaging and two grating observations with combined effective ACIS-S imaging exposures of ~ 190 ks at 0.3–3 keV, ~ 210 ks at 3–6 keV, and ~ 360 ks at higher energies. To exploit the superior Chandra-ACIS spatial resolution, we have made use of subpixel binning up to $1/16$ of the native $0''.492$ pixel size and PSF-based image restoration techniques to separate the emission coming from the different structures observed in both the X-ray and optical bands. Besides the two highly obscured AGNs (Komossa et al. 2003), the highly disturbed central region of NGC 6240 shows different extended X-ray structures (see Figure 2) with counterparts imaged in CO, [O III], and $H\alpha$ line emission (Feruglio et al. 2013a, 2013b; Müller-Sánchez et al. 2018). The ACIS resolution has been

used to characterize the emission mechanisms in different spatial regions (Figures 5, 7, 8) and to image NGC 6240 in different energy bands (Figure 12).

The main results of our analysis of this extended emission are:

1. The spectra extracted from the two nuclear regions ($r < 3$) are significantly harder and have larger absorption with respect to the spectra from the outer regions. The emission from the nuclear regions is dominated by Ne X and Fe XVII lines and at higher energies by Mg XI, Si XIII, and S XV, indicating contribution to the X-ray emission in the circumnuclear region from starburst-driven winds (Feruglio et al. 2013b; Wang et al. 2014). The spectral analysis reveals a hot gas component with $kT \sim 2.3$ keV and a mildly photoionized phase with $\log(U) \sim 0$ in the northern nucleus, while in the southern nucleus we find a thermal gas with $kT \sim 1.9$ keV and two photoionization components with $\log(U) \sim -1$ and $\log(U) \sim 1.4$. The thermal gas has a mean density of ~ 0.4 cm^{-3} . Consistent with the higher absorbing column estimated for the northern nucleus, its circumnuclear emission is detected at energies > 1.6 keV, while for the southern nucleus this

emission is already visible above 0.95 keV, extending toward the WS extension.

2. The surface brightness profiles extracted in different directions show a broken power-law shape, flatter on the interior, and steeper in the outer regions. This suggests the presence of a freely expanding wind in the outer regions and some form of hot plasma confinement in the inner region, within ~ 2.5 kpc ($r < 5''$). If the confinement is magnetic, magnetic fields of $\sim 100 \mu\text{G}$ would be required, similar to those measured in the outflow of M82 (Lopez-Rodriguez et al. 2021).
3. The [O III] to soft X-ray flux ratio profiles are compatible with the values measured for NGC 4151 at small radii, while for $r > 5''$ the decreasing X-ray flux yields values of this ratio of ~ 100 . The thermal gas at $kT \sim 1$ keV at large radii may absorb soft X-rays from the AGN but not the extreme ultraviolet radiation leading to a rapid increase in $F_{[\text{O III}]} / F_{0.5-2}$ beyond ~ 2.5 kpc, where $N_{\text{H}} \sim 3 \times 10^{21} \text{ cm}^{-2}$ radially.
4. The outer outflow [O III] region and the outflow ridge perpendicular to the outflow axis are more prominent below 1.15 keV and are dominated by O VII, O VIII, Ne IX, and Ne X emission lines, as observed in nearby Seyfert galaxies, and are related to shock excitation. Spectral analysis indicates in these regions the presence of a ~ 1 keV thermal gas, together with two photoionized components with $\log U \sim 0$ and $\log U \sim 2$. The arc in the SW (Figure 14) could be connected with the other side of the bicone.
5. The X-ray emission from the NW loop H α region peaks between 0.7 and 1.15 keV, but it is also detected at higher energies, showing Mg XI, Si XIII, and S XV lines, which are usually associated with starburst activity. The spectrum from this region is best fitted by a two-temperature, ~ 0.8 and ~ 1.8 keV, thermal gas, with an additional highly photoionized phase with $\log(U) \sim 1.3$.
6. The ES extension and the WS extension regions are dominated by O VIII, Fe XX, and Ne X emission. The spectral analysis indicates the presence of a thermal gas component with $kT \sim 1$ keV and a mildly photoionized component with $\log(U) \sim 0$, possibly connected with the same component observed in the northern nucleus. If this feature is the southern side of a biconical outflow from the northern CT AGN, the northern side could be obscured by the dusty galactic disk (see Müller-Sánchez et al. 2018).
7. The iron abundance of thermal components is found to be about solar in the nuclear regions and subsolar in the outer regions. The ratio of α elements over Fe abundances are compatible with SN II yields but not with SN Ia yields, confirming the importance of active star formation in NGC 6240 and giving a direct view of the enrichment of the ISM in the NGC 6240 system.

The emission from NGC 6240 is complex, and different physical processes are at work in this source. The results of this

analysis confirm the significant contribution of starburst-driven winds to the X-ray emission observed in this source, in particular in the central region and in the NW H α loop. The [O III] outer outflow and the outflow ridge regions are likely due to both photoionization and shock excitation, connected with the southern nucleus activity, while the southern protrusions may indicate the edges of an ionization cone connected with the northern nucleus activity.

Figure 16 sums up our interpretation of the extended X-ray emission observed in NGC 6240, with the red dashed lines delineating the edges of the ionization cone emerging from the northern nucleus, the yellow dashed lines indicating the edges of the ionization cone linked to the southern nucleus (with a putative, weak counter-cone extending to the west), and the dashed magenta lines marking the starburst-driven winds extending in the NW H α loop.

As the nearest double-AGN merging galaxy system, NGC 6240 is a unique source that provides a complex mix of different physical processes that can be used to study the galaxy–black hole evolution and interaction.

We thank the anonymous referee for their useful comments and suggestions. This work is supported by the “Departments of Excellence 2018–2022” Grant awarded by the Italian Ministry of Education, University and Research (MIUR) (L. 232/2016). A.P. acknowledges financial support from the Consorzio Interuniversitario per la Fisica Spaziale (CIFS) under the agreement related to the grant MASF_CONTR_FIN_18_02. J.W. acknowledges support from NSFC grants U1831205 and 12033004. This work was partially supported by NASA contract NAS8-03060 (CXC). This research has made use of data obtained from the Chandra Data Archive. This research is based on observations made with the NASA/ESA Hubble Space Telescope, obtained from the data archive at the Space Telescope Science Institute. STScI is operated by the Association of Universities for Research in Astronomy, Inc. under NASA contract NAS5-26555. This research has made use of software provided by the Chandra X-ray Center (CXC) in the application packages CIAO, ChIPS, and Sherpa.

Software: CIAO (Fruscione et al. 2006), Sherpa (Freeman et al. 2001; Doe et al. 2007; Burke et al. 2020), ChiPS (Germain et al. 2006), Cloudy (c08.01 Ferland et al. 1998), XSPEC (Arnaud 1996).

Appendix Spectral Fits for Physical Models

In this appendix we present the full set of physical models—that is, comprising thermal and photoionization components—used to fit the spectra extracted in the regions presented in Figure 5. All the models considered here are listed in Table 4. The models that we selected as best fits on the basis of fit statistics and residual distribution are indicated in boldface.

Table 4
Full List of the Best-fit Results of the Spectra Extracted in the Regions Presented in Figure 5 for the Physical Models Comprising the Thermal and Photoionization Components (see Section 4)

	N Nuclear			S Nuclear				Central							
kT_1 (keV)	$0.87^{+0.04}_{-0.05}$	$2.32^{+1.41}_{-0.58}$	$0.69^{+0.08}_{-0.12}$	$1.64^{+0.06}_{-0.07}$	$0.98^{+0.06}_{-0.06}$	$1.56^{+0.07}_{-0.08}$	$1.88^{+1.13}_{-0.21}$	$1.54^{+0.08}_{-0.08}$	$1.08^{+0.27}_{-0.10}$	$1.45^{+0.11}_{-0.15}$	$1.18^{+0.16}_{-0.18}$	$1.31^{+0.18}_{-0.08}$			
kT_2 (keV)					$6.48^{+1.64}_{-1.29}$				> 2.14		< 1.00				
Fe	$0.07^{+0.02}_{-0.02}$	$1.22^{+4.35}_{-0.75}$	1.8^*	$0.10^{+0.04}_{-0.04}$	$2.89^{+4.97}_{-2.80}$	$0.45^{+0.18}_{-0.13}$	1.0^*	$0.08^{+0.04}_{-0.04}$	$0.14^{+0.12}_{-0.08}$	$0.22^{+0.11}_{-0.07}$	$0.23^{+0.13}_{-0.09}$	$0.63^{+0.92}_{-0.31}$			
α /Fe	$5.95^{+1.38}_{-1.07}$	$3.51^{+1.72}_{-1.05}$	< 0.40	$9.65^{+5.08}_{-4.78}$	$2.15^{+9.55}_{-0.78}$	$3.17^{+0.76}_{-0.58}$	$2.57^{+0.60}_{-1.32}$	$11.22^{+2.69}_{-3.47}$	$6.66^{+6.20}_{-2.68}$	$5.06^{+1.86}_{-1.29}$	$4.76^{+2.39}_{-1.23}$	$2.45^{+1.43}_{-0.78}$			
$\log(U_1)$	$0.00^{+0.03}_{-0.12}$	$0.00^{+0.05}_{-0.10}$	$-0.06^{+0.12}_{-0.47}$			$-0.16^{+0.07}_{-0.05}$	$-0.08^{+0.10}_{-0.11}$			$-0.19^{+0.09}_{-0.05}$	$-0.01^{+0.18}_{-0.19}$	$-0.15^{+0.49}_{-0.50}$	$-0.18^{+0.21}_{-0.12}$		
$\log(N_{H1})$		22.3^*	22.4^*	$22.29^{+0.24}_{-0.45}$		$20.00^{+0.32}_{-0.46}$	22.5^*			19.8^*	22.5^*	$22.56^{+0.65}_{-0.55}$	19.2^*		
$\log(U_2)$		2.0^*		2.0^*		$1.77^{+0.05}_{-0.12}$				$1.43^{+0.12}_{-0.09}$		$1.67^{+0.05}_{-0.05}$	1.5^*		
$\log(N_{H2})$		20.9^*		20.9^*		19.0^*				20.1^*		$20.40^{+0.33}_{-0.56}$	22.3^*		
N_H (10^{22} cm $^{-2}$)	$0.11^{+0.04}_{-0.02}$	$1.19^{+0.05}_{-0.05}$	$1.13^{+0.10}_{-0.07}$	$1.68^{+0.20}_{-0.20}$	$0.60^{+0.03}_{-0.03}$	$0.72^{+0.19}_{-0.10}$	$1.15^{+0.09}_{-0.06}$	$0.72^{+0.04}_{-0.04}$	$0.69^{+0.16}_{-0.04}$	$0.59^{+0.04}_{-0.03}$	$0.64^{+0.09}_{-0.12}$	$1.10^{+0.05}_{-0.04}$	$0.68^{+0.05}_{-0.04}$	$0.68^{+0.06}_{-0.05}$	$1.04^{+0.08}_{-0.10}$
χ^2 (d.o.f.)	$0.85(81)$	$1.01(82)$	$1.04(79)$	$0.96(78)$	$1.18(124)$	$0.81(122)$	$0.78(123)$	$0.79(122)$	$0.74(120)$	$0.84(112)$	$0.72(110)$	$0.71(111)$	$0.70(110)$	$0.69(107)$	$0.69(109)$

	Outflow Ridge				Outer Outflow				NES Extension									
kT_1 (keV)	$0.90^{+0.05}_{-0.05}$	$0.86^{+0.08}_{-0.07}$	$1.02^{+0.06}_{-0.08}$	$0.86^{+0.09}_{-0.08}$	$0.88^{+0.12}_{-0.06}$	$0.85^{+0.11}_{-0.03}$	$0.77^{+0.07}_{-0.24}$	$0.81^{+0.04}_{-0.04}$	$0.61^{+0.18}_{-0.21}$	$0.80^{+0.04}_{-0.04}$	$0.67^{+0.12}_{-0.09}$	$1.78^{+0.23}_{-0.40}$	$0.84^{+0.19}_{-0.11}$	$1.55^{+0.14}_{-0.16}$	$0.88^{+0.40}_{-0.14}$	$0.72^{+0.08}_{-0.10}$		
kT_2 (keV)		$1.56^{+0.29}_{-0.22}$		$1.40^{+0.38}_{-0.17}$		$1.16^{+0.63}_{-0.63}$		$1.03^{+0.22}_{-0.08}$			$1.14^{+0.16}_{-0.16}$		$2.15^{+0.58}_{-0.29}$	$2.07^{+0.42}_{-0.42}$				
Fe	$0.06^{+0.03}_{-0.02}$	$0.15^{+0.20}_{-0.05}$	$0.10^{+0.09}_{-0.04}$	$0.17^{+0.23}_{-0.05}$	$0.11^{+0.08}_{-0.05}$	$0.12^{+0.10}_{-0.04}$	$0.21^{+0.08}_{-0.06}$	$0.16^{+0.06}_{-0.15}$	$0.37^{+0.32}_{-0.15}$	$0.21^{+0.14}_{-0.07}$	$0.35^{+0.30}_{-0.14}$	$0.09^{+0.08}_{-0.09}$	$0.33^{+0.28}_{-0.28}$	$0.14^{+0.13}_{-0.09}$	$0.29^{+0.30}_{-0.20}$	$0.67^{+1.29}_{-0.37}$		
α /Fe	$9.91^{+4.60}_{-2.70}$	$5.61^{+1.48}_{-1.91}$	$7.39^{+3.22}_{-3.07}$	$5.01^{+9.90}_{-1.67}$	$6.56^{+3.52}_{-2.03}$	$4.98^{+0.76}_{-0.69}$	$3.84^{+0.74}_{-0.62}$	$4.49^{+0.80}_{-0.74}$	$2.80^{+0.96}_{-0.73}$	$4.02^{+0.85}_{-0.72}$	$2.99^{+0.89}_{-0.74}$	$10.87^{+8.23}_{-4.78}$	$2.45^{+3.44}_{-1.19}$	$6.51^{+8.27}_{-2.65}$	$2.98^{+5.55}_{-1.63}$	$0.55^{+0.50}_{-0.28}$		
$\log(U_1)$			$1.17^{+0.09}_{-0.39}$	$0.25^{+0.12}_{-0.29}$	0.1^{**}	$0.08^{+0.33}_{-0.58}$		1.9^*	$-1.45^{+0.40}_{-0.31}$	$-0.50^{+0.78}_{-0.68}$	-0.6^*			$-0.15^{+0.16}_{-0.08}$	$0.10^{+0.34}_{-0.26}$	-0.2^{**}	-0.5^{**}	
$\log(N_{H1})$			19.5^*	$21.26^{+1.17}_{-1.69}$	20.3^{**}	21.7^*		19.7^*	19.0^*	22.2^*	22.2^*			19.9^*	22.5^*	22.5^{**}	20.4^{**}	
$\log(U_2)$		2.0^*				2.0^*				1.9^*	2.2^{**}			1.7^*			1.9^*	
$\log(N_{H2})$			$21.41^{+0.31}_{-0.42}$			19.0^*				19.7^*	22.9^{**}			20.6^*			21.2^*	
N_H (10^{22} cm $^{-2}$)	$0.31^{+0.04}_{-0.04}$	$0.31^{+0.05}_{-0.04}$	$0.32^{+0.05}_{-0.05}$	$0.39^{+0.13}_{-0.06}$	$0.39^{+0.07}_{-0.10}$	$0.38^{+0.05}_{-0.05}$	$0.08^{+0.02}_{-0.05}$	$0.06^{+0.03}_{-0.02}$	$0.07^{+0.02}_{-0.02}$	$0.16^{+0.06}_{-0.07}$	$0.09^{+0.03}_{-0.03}$	$0.10^{+0.04}_{-0.03}$	$0.39^{+0.12}_{-0.04}$	$0.68^{+0.21}_{-0.18}$	$0.98^{+0.06}_{-0.06}$	$0.52^{+0.08}_{-0.07}$	$0.62^{+0.25}_{-0.16}$	$1.04^{+0.16}_{-0.15}$
χ^2 (d.o.f.)	$0.76(69)$	$0.70(67)$	$0.99(69)$	$0.74(66)$	$0.70(66)$	$0.71(66)$	$0.73(74)$	$0.67(72)$	$0.69(73)$	$0.66(70)$	$0.68(71)$	$0.66(70)$	$0.82(58)$	$0.72(56)$	$0.76(59)$	$0.74(56)$	$0.73(55)$	$0.68(56)$

	ES Extension				WS Extension				W Filament				NW Loop													
kT_1 (keV)	$0.87^{+0.04}_{-0.05}$	$0.84^{+0.07}_{-0.04}$	$0.81^{+0.05}_{-0.06}$	$0.92^{+0.06}_{-0.22}$	$0.68^{+0.17}_{-0.16}$	$0.94^{+0.04}_{-0.04}$	$0.86^{+0.05}_{-0.04}$	$1.04^{+0.28}_{-0.08}$	$0.85^{+0.08}_{-0.04}$	$1.02^{+0.30}_{-0.05}$	$0.75^{+0.06}_{-0.04}$	$0.77^{+0.05}_{-0.06}$	$0.78^{+0.06}_{-0.06}$	$0.52^{+0.19}_{-0.16}$	$0.76^{+0.05}_{-0.05}$	$0.54^{+0.21}_{-0.14}$	$0.95^{+0.03}_{-0.03}$	$0.82^{+0.05}_{-0.05}$	$1.11^{+0.07}_{-0.14}$	$0.82^{+0.11}_{-0.08}$	$1.27^{+0.16}_{-0.11}$	$0.70^{+0.14}_{-0.16}$				
kT_2 (keV)			> 0.87		$1.13^{+0.45}_{-0.45}$		$1.98^{+0.36}_{-0.28}$		$1.49^{+0.46}_{-0.42}$		$2.16^{+5.33}_{-0.52}$		$0.98^{+0.23}_{-0.29}$	$0.97^{+0.43}_{-0.17}$	$1.80^{+0.28}_{-0.21}$			$1.82^{+0.28}_{-0.28}$			$1.50^{+0.38}_{-0.38}$					
Fe	$0.07^{+0.02}_{-0.02}$	$0.12^{+0.03}_{-0.03}$	$0.18^{+0.09}_{-0.05}$	$0.16^{+0.08}_{-0.05}$	$0.19^{+0.16}_{-0.08}$	$0.07^{+0.02}_{-0.02}$	$0.39^{+0.21}_{-0.14}$	$0.23^{+0.16}_{-0.08}$	> 0.84	$0.16^{+2.15}_{-0.05}$	$0.10^{+0.04}_{-0.04}$	$0.27^{+0.27}_{-0.14}$	$0.22^{+0.41}_{-0.09}$	$0.56^{+1.55}_{-0.31}$	> 1.77	> 0.73	$0.07^{+0.02}_{-0.02}$	$0.21^{+0.08}_{-0.08}$	$0.26^{+0.14}_{-0.14}$	$0.34^{+0.24}_{-0.18}$	$0.35^{+0.64}_{-0.18}$	$0.50^{+1.42}_{-0.28}$				
α /Fe	$5.80^{+1.25}_{-1.01}$	$3.89^{+0.84}_{-0.71}$	$3.36^{+0.87}_{-0.68}$	$3.42^{+1.14}_{-0.82}$	$3.01^{+1.12}_{-0.88}$	$5.03^{+1.18}_{-0.96}$	$2.29^{+0.60}_{-0.50}$	$2.89^{+0.80}_{-0.76}$	$1.49^{+0.46}_{-0.42}$	$3.07^{+0.96}_{-0.98}$	$4.25^{+1.28}_{-1.03}$	$3.09^{+0.99}_{-0.81}$	$2.46^{+1.11}_{-1.05}$	$1.77^{+0.84}_{-0.83}$	$1.77^{+1.02}_{-0.74}$	$1.99^{+0.87}_{-1.06}$	$9.52^{+2.25}_{-1.78}$	$5.53^{+1.26}_{-0.96}$	$5.76^{+1.73}_{-1.11}$	$4.82^{+1.22}_{-0.92}$	$4.90^{+2.29}_{-1.71}$	$4.36^{+1.88}_{-1.22}$				
$\log(U_1)$		$1.09^{+0.05}_{-0.04}$	$-0.50^{+0.28}_{-0.24}$	$-0.35^{+0.41}_{-0.33}$	$-0.53^{+0.21}_{-0.30}$	$-0.38^{+0.33}_{-0.29}$		$1.06^{+0.06}_{-0.05}$	$0.26^{+0.06}_{-0.16}$	$1.45^{+0.15}_{-0.14}$	$-2.00^{+0.39}_{-0.33}$	$0.07^{+0.11}_{-0.07}$	$-0.75^{+0.37}_{-0.08}$	-1.0^*	$-0.75^{+0.53}_{-0.72}$	-3.0^*		$0.00^{+0.07}_{-0.06}$	$0.33^{+0.14}_{-0.14}$	$1.25^{+0.12}_{-0.12}$	$-0.82^{+0.66}_{-0.42}$	-1.3^*				
$\log(N_{H1})$		19.7^*	22.9^*	23.5^*	22.9^*	23.2^*		19.8^*	$20.20^{+0.28}_{-0.30}$	19.9^*	21.0^*		$20.02^{+0.31}_{-0.21}$	$20.68^{+0.81}_{-1.46}$	19.0^*	20.3^*	21.9^*		$20.20^{+0.30}_{-0.30}$	20.5^*	22.1^*	$20.70^{+0.74}_{-0.70}$	20.4^*			
$\log(U_2)$		2.0^*			$0.85^{+0.25}_{-0.25}$	1.2^*		2.0^*	$0.75^{+0.12}_{-0.23}$				$1.59^{+0.09}_{-0.07}$	$1.76^{+0.15}_{-0.12}$	1.8^*			$1.54^{+0.64}_{-0.64}$		$1.09^{+0.08}_{-0.07}$	$1.31^{+0.14}_{-0.14}$					
$\log(N_{H2})$			22.1^*		19.4^*			$21.23^{+0.35}_{-0.35}$		20.8^*			19.0^*		22.3^*	22.2^*			$20.72^{+0.18}_{-0.20}$			19.7^*	$20.50^{+0.95}_{-0.95}$			
N_H (10^{22} cm $^{-2}$)	$0.12^{+0.03}_{-0.02}$	$0.12^{+0.02}_{-0.02}$	$0.18^{+0.03}_{-0.03}$	$0.17^{+0.05}_{-0.05}$	$0.20^{+0.04}_{-0.05}$	$0.18^{+0.04}_{-0.05}$	$0.13^{+0.03}_{-0.02}$	$0.40^{+0.05}_{-0.05}$	$0.13^{+0.03}_{-0.03}$	$0.22^{+0.05}_{-0.05}$	$0.19^{+0.05}_{-0.04}$	$0.14^{+0.06}_{-0.06}$	$0.41^{+0.04}_{-0.04}$	$0.29^{+0.12}_{-0.15}$	$0.32^{+0.08}_{-0.11}$	$0.21^{+0.11}_{-0.12}$	$0.13^{+0.07}_{-0.07}$	$0.34^{+0.03}_{-0.03}$	$0.35^{+0.04}_{-0.04}$	$0.57^{+0.03}_{-0.03}$	$0.51^{+0.05}_{-0.04}$	$0.34^{+0.04}_{-0.04}$	$0.46^{+0.06}_{-0.06}$	$0.41^{+0.05}_{-0.05}$		
χ^2 (d.o.f.)	$0.85(83)$	$0.99(84)$	$0.65(81)$	$0.65(79)$	$0.65(79)$	$0.64(76)$	$0.93(84)$	$0.67(82)$	$0.73(84)$	$0.76(81)$	$0.58(80)$	$0.79(80)$	$0.73(45)$	$0.63(43)$	$1.12(44)$	$0.68(42)$	$0.60(42)$	$0.57(41)$	$0.55(41)$	$0.94(102)$	$0.76(100)$	$1.11(100)$	$0.81(100)$	$0.72(98)$	$0.73(97)$	$0.72(96)$

Note. Only models with a reduced $\chi^2 < 1.2$ are shown. For each region, we present the temperature of the first (kT_1) and second (kT_2) thermal components, the iron abundance (Fe), and the abundance ratio of α elements to iron (α /Fe), both linked between the two thermal components, the ionization parameter of the first (U_1) and second (U_2) ionization components, the hydrogen column density of the first (N_{H1}) and second (N_{H2}) ionization components, an additional intrinsic hydrogen column density (N_H), and the reduced χ^2 (with degrees of freedom indicated in parentheses). Parameters marked with an asterisk (*) could not be constrained and were frozen to their best-fit values. Parameters with two asterisks (**) indicate a parameter frozen to its best-fit value and whose component normalization is only constrained with an upper limit. In boldface we indicate the best-fit models, selected on the basis of fit statistics and residual distribution.

ORCID iDs

A. Paggi  <https://orcid.org/0000-0002-5646-2410>
 G. Fabbiano  <https://orcid.org/0000-0002-3554-3318>
 E. Nardini  <https://orcid.org/0000-0001-9226-8992>
 M. Karovska  <https://orcid.org/0000-0003-1769-9201>
 M. Elvis  <https://orcid.org/0000-0001-5060-1398>
 J. Wang  <https://orcid.org/0000-0003-4874-0369>

References

- Arnaud, K. A. 1996, in *Astronomical Data Analysis Software and Systems V*, ASP Conf. Ser. 101, ed. G. H. Jacoby & J. Barnes (San Francisco, CA: ASP), 17
- Baldi, A., Raymond, J. C., Fabbiano, G., et al. 2006a, *ApJS*, 162, 113
- Baldi, A., Raymond, J. C., Fabbiano, G., et al. 2006b, *ApJ*, 636, 158
- Bennett, C. L., Larson, D., Weiland, J. L., et al. 2014, *ApJ*, 794, 135
- Bianchi, S., Chiaberge, M., Evans, D. A., et al. 2010, *MNRAS*, 405, 553
- Bianchi, S., Guainazzi, M., & Chiaberge, M. 2006, *A&A*, 448, 499
- Burke, D., Laurino, O., & Wmclaugh 2020, *sherpa/sherpa*: Sherpa v4.12.1, Zenodo, doi:10.5281/zenodo.3944985
- Croston, J. H., Hardcastle, M. J., Harris, D. E., et al. 2005, *ApJ*, 626, 733
- Doe, S., Nguyen, D., Stawarz, C., et al. 2007, in *Astronomical Data Analysis Software and Systems XVI* ASP Conf. Ser. 376, ed. R. A. Shaw (San Francisco, CA: ASP), 543
- Downes, D., Solomon, P. M., & Radford, S. J. E. 1993, *ApJL*, 414, L13
- Engel, H., Davies, R. I., Genzel, R., et al. 2010, *A&A*, 524, A56
- Esch, D. N., Connors, A., Karovska, M., et al. 2004, *ApJ*, 610, 1213
- Fabbiano, G. 1988, *ApJ*, 330, 672
- Fabbiano, G., & Elvis, M. 2019, *ApJ*, 884, 163
- Fabbiano, G., Elvis, M., Paggi, A., et al. 2017, *ApJL*, 842, L4
- Fabbiano, G., Paggi, A., Karovska, M., et al. 2018, *ApJ*, 865, 83
- Fabbiano, G., Paggi, A., Karovska, M., et al. 2020, *ApJ*, 902, 49
- Fabbiano, G., Siemiginowska, A., Paggi, A., et al. 2019, *ApJ*, 870, 69
- Ferland, G. J., Korista, K. T., Verner, D. A., et al. 1998, *PASP*, 110, 761
- Feruglio, C., Fiore, F., Maiolino, R., et al. 2013a, *A&A*, 549, A51
- Feruglio, C., Fiore, F., Piconcelli, E., et al. 2013b, *A&A*, 558, A87
- Fosbury, R. A. E., & Wall, J. V. 1979, *MNRAS*, 189, 79
- Freeman, P., Doe, S., & Siemiginowska, A. 2001, *Proc. SPIE*, 4477, 76
- Fried, J. W., & Schulz, H. 1983, *A&A*, 118, 166
- Fruchter, A. S., & Hook, R. N. 2002, *PASP*, 114, 144
- Fruscione, A., McDowell, J. C., Allen, G. E., et al. 2006, *Proc. SPIE*, 6270, 62701V
- Gallimore, J. F., & Beswick, R. 2004, *AJ*, 127, 239
- Genzel, R., Lutz, D., & Tacconi, L. 1998, *Natur*, 395, 859
- Germain, G., Milaszewski, R., McLaughlin, W., et al. 2006, in *Astronomical Data Analysis Software and Systems XV* ASP Conf. Ser. 351, ed. C. Gabriel et al. (San Francisco, CA: ASP), 57
- Gerssen, J., van der Marel, R. P., Axon, D., et al. 2004, *AJ*, 127, 75
- Halpern, J. P. 1984, *ApJ*, 281, 90
- Harris, D. E., Mossman, A. E., & Walker, R. C. 2004, *ApJ*, 615, 161
- Heckman, T. M., Armus, L., & Miley, G. K. 1987, *AJ*, 93, 276
- HI4PI Collaboration, Ben Bekhti, N., Flöer, L., et al. 2016, *A&A*, 594, A116
- Humphrey, P. J., & Buote, D. A. 2006, *ApJ*, 639, 136
- Jones, M. L., Parker, K., Fabbiano, G., et al. 2021, *ApJ*, 910, 19
- Karovska, M., Carilli, C. L., Raymond, J. C., et al. 2007, *ApJ*, 661, 1048
- Karovska, M., Gaetz, T. J., Carilli, C. L., et al. 2010, *ApJL*, 710, L132
- Karovska, M., Schlegel, E., Hack, W., et al. 2005, *ApJL*, 623, L137
- Komossa, S., Burwitz, V., Hasinger, G., et al. 2003, *ApJL*, 582, L15
- Levenson, N. A., Heckman, T. M., Krolik, J. H., et al. 2006, *ApJ*, 648, 111
- Lira, P., Ward, M. J., Zezas, A., et al. 2002, *MNRAS*, 333, 709
- Lopez-Rodriguez, E., Guerra, J. A., Asgari-Targhi, M., et al. 2021, *ApJ*, 914, 24
- Ma, J., Elvis, M., Fabbiano, G., et al. 2020, *ApJ*, 900, 164
- Maksym, W. P., Fabbiano, G., Elvis, M., et al. 2019, *ApJ*, 872, 94
- Marinucci, A., Bianchi, S., Matt, G., et al. 2011, *A&A*, 526, A36
- Müller-Sánchez, F., Nevin, R., Comerford, J. M., et al. 2018, *Natur*, 556, 345
- Nardini, E. 2017, *MNRAS*, 471, 3483
- Nardini, E., Wang, J., Fabbiano, G., et al. 2013, *ApJ*, 765, 141
- Paggi, A., Wang, J., Fabbiano, G., et al. 2012, *ApJ*, 756, 39
- Persic, M., & Rephaeli, Y. 2002, *A&A*, 382, 843
- Richings, A. J., Fabbiano, G., Wang, J., et al. 2010, *ApJ*, 723, 1375
- Schurch, N. J., Roberts, T. P., & Warwick, R. S. 2002, *MNRAS*, 335, 241
- Scoville, N. Z., Evans, A. S., Thompson, R., et al. 2000, *AJ*, 119, 991
- Siemiginowska, A., Stawarz, L., Cheung, C. C., et al. 2007, *ApJ*, 657, 145
- Simionescu, A., Werner, N., Finoguenov, A., et al. 2008, *A&A*, 482, 97
- Tacconi, L. J., Genzel, R., Tecza, M., et al. 1999, *Ap&SS*, 266, 157
- Travascio, A., Fabbiano, G., Paggi, A., et al. 2021, *ApJ*, 921, 129
- Treister, E., Messias, H., Privon, G. C., et al. 2020, *ApJ*, 890, 149
- Wang, J., Fabbiano, G., Elvis, M., et al. 2011a, *ApJ*, 736, 62
- Wang, J., Fabbiano, G., Elvis, M., et al. 2011b, *ApJ*, 742, 23
- Wang, J., Fabbiano, G., Karovska, M., et al. 2009, *ApJ*, 704, 1195
- Wang, J., Fabbiano, G., Risaliti, G., et al. 2010, *ApJL*, 719, L208
- Wang, J., Fabbiano, G., Risaliti, G., et al. 2011c, *ApJ*, 729, 75
- Wang, J., Nardini, E., Fabbiano, G., et al. 2014, *ApJ*, 781, 55
- Yoshida, M., Yagi, M., Ohyama, Y., et al. 2016, *ApJ*, 820, 48